Coupled electro-chemo-elasticity: Application to modeling the actuation response of ionic polymer–metal composites

Coupled electro-chemo-elasticity: application to modeling the actuation response of ionic polymer-metal composites

Sooraj Narayan, Eric M. Stewart, and Lallit Anand*
Department of Mechanical Engineering
Massachusetts Institute of Technology
Cambridge, MA 02139, USA

Abstract

We have formulated a large deformation thermodynamically-consistent electro-chemo-elasticity theory for modeling the actuation response of ionic polymer-metal composites. Our theory accounts for the simultaneous evolution of the electric potential, the concentration of the mobile hydrated cations, and the deformation of the host ionic polymer matrix. We have numerically implemented our theory in an implicit finite element program. We use this simulation capability to first calibrate the material parameters in the theory for a Nafion-based ionic polymer-metal composite, and then validate our theory by comparing predictions from the theory against other experimental data available in the literature. We also demonstrate the utility of our simulation capability by conducting full three-dimensional simulations of two soft-robotics applications with some geometric complexity: (i) a biomimetic fin, and (ii) a micro-gripper.

Keywords: electro-chemo-elasticity; ionic polymer-metal composites; soft-robotics; finite-element simulations.

1 Introduction

Synthetic polymers with ionic properties are called ionomers. A prominent example of an ionomeric polymer is Nafion.[1] It is made up of crosslinked polymer chains which have a backbone of a perfluorinated copolymer of poly-tetrafluoroethylene, with regularly spaced long per-fluorovinyl ether pendant side chains that terminate in negatively-charged ionic sulfonate groups (anions). Nafion membranes are permeable to water or other polar solvents and contain mobile positively-charged ions (cations) that move within the perfluorinated backbone. Ionic polymer-metal composites (IPMCs) consist of membranes of ionic polymers ($\approx 200\,\mu$m thick), with noble metal electrodes (≈ 5 to $10\,\mu$m thick) plated on both faces of the membrane. The matrix of an IPMC is solvated with a suitable solvent, and neutralized with an amount of cations (e.g., Li^+, Na^+, K^+, or H^+) which balance the charge of the anions that are covalently fixed to the polymer chains.

When a solvated IPMC membrane is stimulated with a suddenly applied small step potential (≈ 1 to $3\,$V), both the anions and cations are subjected to an electric field. While the anions remain fixed to the polymer chains, the mobile cations migrate toward the cathode, transporting with them some solvent molecules due to hydration effects. The redistribution of hydrated cations causes a differential swelling of the membrane, and the resulting gradient in the volumetric deformation across the thickness of the membrane causes the IPMC to bend. A schematic of this actuation mechanism is shown in Fig. 1. Under an alternating potential, a cantilevered strip of an IPMC performs bending oscillations at the frequency of the applied voltage, usually no more than a few to a few tens of hertz. When an IPMC membrane is suddenly bent, a small voltage of

*Corresponding author. Tel.: +1-617-253-1635; E-mail address: anand@mit.edu
[1]Nafion is a brand name of the Chemours company.

the order of millivolts is produced across its faces. Hence, IPMCs can serve as soft actuators and sensors (cf., e.g., Shahinpoor and Kim, 2001; Nemat-Nasser, 2008; Jo et al., 2013).[2]

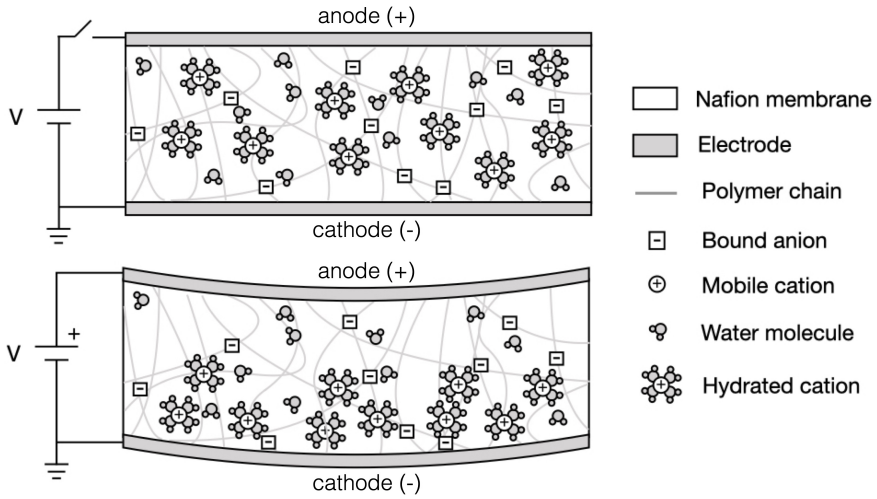

Figure 1: Schematic of the actuation mechanism under a step voltage input of an IPMC membrane due to the migration of hydrated cations.

The low actuation voltage and high compliance of IPMCs make them excellent candidates for use as actuators in both wet and dry environments. They can serve as "artificial muscles" for use in a wide range of soft-robotics and biomimetic applications (Minaian et al., 2021). The use of ionic polymers as actuators was first proposed by Oguro et al. (1992). Subsequent efforts towards understanding the underlying physical mechanisms of IPMCs were led by the experiments performed and models proposed by Shahinpoor and Kim (Shahinpoor and Kim, 2001; Kim and Shahinpoor, 2003; Shahinpoor and Kim, 2004), and Nemat-Nasser and co-workers (Nemat-Nasser and Li, 2000; Nemat-Nasser, 2002). For a more comprehensive discussion of the early experimental and modeling literature on IPMCs, see the book chapters by Nemat-Nasser and Thomas (2004) and Nemat-Nasser (2008), and the references cited therein.

While the underlying physical mechanism behind the actuation and sensing response of IPMCs is reasonably well understood and agreed upon for some time, viz. *migration of mobile hydrated cations under the gradient of an electric potential*, the continuum-mechanical modeling of the coupled chemo-electro-mechanical response of IPMCs in a thermo-dynamically consistent fashion has been a more recent effort in the literature. Examples are the papers by Nardinocchi and co-workers (cf., e.g., Nardinocchi et al., 2011; Galante et al., 2013; Nardinocchi and Pezzulla, 2013; Nardinocchi et al., 2014) and Wallmersperger and co-workers (cf., e.g., Rossi and Wallmersperger, 2018; Rossi et al., 2018). Also see Cha and Porfiri (2014), Porfiri et al. (2017), and Leronni and Bardella (2021). Some of these authors have numerically implemented their theories, and have reported on simulations of the bending of cantilevered beams made from IPMCs. However, reports of comparisons of the predictions of the theories against physical experiments are quite limited.

The purpose of this paper is to report on:

- Our formulation of a thermodynamically consistent large-deformation continuum mechanical theory for coupled electro-chemo-mechanics.[3]
- The numerical implementation of this theory in a finite element program.
- Use of this simulation capability to first calibrate the material parameters in our theory, and subsequently to validate the theory by comparing the predictions of the theory against data from physical

[2]Nafion membranes are also widely employed in micro-batteries and proton-exchange-membrane fuel cells. In this paper we concentrate on modeling their response in IPMCs as actuators.

[3]Our theory is similar to that in the work of Nardinocchi and co-workers (Nardinocchi et al., 2011; Galante et al., 2013), but it differs in several details which are too many to enumerate here.

experiments on Nafion-based IPMCs available in the literature.

- Demonstrate the utility of our numerical simulation capability by conducting simulations pertinent to some soft-robotics applications.

In formulating our theory we have made the following major modeling assumptions:

- The polymer-solvent-ions mixture is treated as a single homogenized continuum body allowing for a mass flux to be carried by the mobile hydrated cations.
- Since the neutral solvent (water) molecules diffuse slowly, we neglect the effects of solvent diffusion in the membrane.[4]
- Further, since the motion of the cations occurs at time scales considerably longer than those associated with wave propagation in solids, all inertial effects are neglected.
- Accordingly, only the electrostatic version of the Maxwell equations is employed.

The paper is organized as follows. We formulate our theory in Section 2. We have implemented the theory as a user element subroutine (UEL) in the implicit finite element program Abaqus/Standard (Abaqus, 2017). Using this numerical implementation in Section 3 we conduct numerical simulations to calibrate the material parameters for a Nafion-based IPMC, and then we validate the theory by comparing the predictions of the theory against data from other physical experiments available in the literature. To demonstrate the robustness of our numerical simulation capability, in Section 4 we show full three-dimensional simulations of two soft-robotics applications: (i) a biomimetic fin, and (ii) a micro-gripper. We close in Section 5 with some final remarks.

2 Theory

2.1 Basic kinematics

Consider a macroscopically homogeneous body B with the region of space it occupies in a fixed *reference configuration*, and denote by $\mathbf{X}$ an arbitrary material point of B.[5] A motion of B is a smooth one-to-one mapping $\mathbf{x} = \boldsymbol{\chi}(\mathbf{X}, t)$ with deformation gradient and velocity given by

$$\mathbf{F} = \nabla\boldsymbol{\chi}, \quad \mathbf{v} = \dot{\boldsymbol{\chi}}, \quad \mathbf{L} = \operatorname{grad}\mathbf{v} = \dot{\mathbf{F}}\mathbf{F}^{-1}. \tag{2.1}$$

We write

$$J = \det\mathbf{F} > 0, \tag{2.2}$$

so that $\mathbf{F}$ is invertible.

Throughout we denote by P an arbitrary part of the reference body B with $\mathbf{n}_{\mathrm{R}}$ the outward unit normal on the boundary $\partial\mathrm{P}$ of P. Also, we denote by $\mathcal{P}_t = \boldsymbol{\chi}(\mathrm{P}, t)$ the image of P in the deformed body $\mathcal{B}_t = \boldsymbol{\chi}(\mathrm{B}, t)$, with $\mathbf{n}$ the outward unit normal on the boundary $\partial\mathcal{P}_t$ of $\mathcal{P}_t$.

[4] Nafion IPMCs with alkali metal cations invariably first bend towards the anode under a step voltage, and then relax back towards the cathode while the applied voltage is being maintained. In this paper we do not attempt to model this complex phenomena of "back-relaxation" which occurs at long time scales. We leave such a modeling effort to future work.

[5] Notation: We use standard notation of modern continuum mechanics (Gurtin et al., 2010). Specifically: ∇ and Div denote the gradient and divergence with respect to the material point $\mathbf{X}$ in the reference configuration, and $\Delta = \operatorname{Div}\nabla$ denotes the referential Laplace operator; grad div, and div grad denote these operators with respect to the point $\mathbf{x} = \boldsymbol{\chi}(\mathbf{X}, t)$ in the deformed body; a superposed dot denotes the material time-derivative. Throughout, we write $\mathbf{F}^{-1} = (\mathbf{F})^{-1}$, $\mathbf{F}^{-\top} = (\mathbf{F})^{-\top}$, etc. We write $\operatorname{tr}\mathbf{A}$, $\operatorname{sym}\mathbf{A}$, $\operatorname{skw}\mathbf{A}$, $\mathbf{A}_0$, and $\operatorname{sym}_0\mathbf{A}$ respectively, for the trace, symmetric, skew, deviatoric, and symmetric-deviatoric parts of a tensor $\mathbf{A}$. Also, the inner product of tensors $\mathbf{A}$ and $\mathbf{B}$ is denoted by $\mathbf{A}:\mathbf{B}$, and the magnitude of $\mathbf{A}$ by $|\mathbf{A}| = \sqrt{\mathbf{A}:\mathbf{A}}$. As a departure from the usual convention in modern continuum mechanics in which vectors are denoted by lower case bold face letters $\mathbf{a}$, $\mathbf{b}$, etc., we denote the two important electrical vector fields using bold face sans-serif fonts as follows: we write e for the electric field, and d for the electric displacement.

2.2 Balance of forces and moments

Standard considerations of balance of forces and moments, when expressed referentially, give the following results:

(a) There exists a stress tensor $\mathbf{T}_{\mathrm{R}}$, called the Piola stress, such that the surface traction on an oriented element of the surface $\partial\mathrm{P}$ of P, is given by the traction relation

$$\mathbf{t}_{\mathrm{R}}(\mathbf{n}_{\mathrm{R}}) = \mathbf{T}_{\mathrm{R}}\mathbf{n}_{\mathrm{R}}\,. \tag{2.3}$$

(b) $\mathbf{T}_{\mathrm{R}}$ satisfies the macroscopic force balance

$$\mathrm{Div}\,\mathbf{T}_{\mathrm{R}} + \mathbf{b}_{\mathrm{R}} = \mathbf{0}, \tag{2.4}$$

where $\mathbf{b}_{\mathrm{R}}$ represents the conventional body force per unit volume of the reference body.[6]

(c) $\mathbf{T}_{\mathrm{R}}$ obeys the the symmetry condition,

$$\mathbf{T}_{\mathrm{R}}\mathbf{F}^{\top} = \mathbf{F}\mathbf{T}_{\mathrm{R}}^{\top}, \tag{2.5}$$

which represents a balance of moments.

As is standard, the stress measure

$$\mathbf{T} = J^{-1}\mathbf{T}_{\mathrm{R}}\mathbf{F}^{\top}, \tag{2.6}$$

represents the symmetric Cauchy stress, in terms of which:

(a) The surface traction on an oriented element of the surface $\partial\mathcal{P}_t$ of $\mathcal{P}_t$, is given by

$$\mathbf{t}(\mathbf{n}) = \mathbf{T}\mathbf{n}. \tag{2.7}$$

(b) And $\mathbf{T}$ satisfies the macroscopic force balance

$$\mathrm{div}\mathbf{T} + \mathbf{b} = \mathbf{0}, \tag{2.8}$$

where $\mathbf{b}$ represents the conventional body force per unit volume of the deformed body.

Remark. The Cauchy stress $\mathbf{T}$ is often referred to as the *total* stress in the electroelasticity literature. However, we see no need to distinguish between a purely mechanical stress and an electrostatic, or Maxwell, stress. Such a decomposition appears naturally when we consider specific thermodynamically-consistent constitutive equations; cf. Section 2.12.

2.3 Balance of mass and charge of the migrating cations

2.3.1 Balance of mass

Let $c_{\mathrm{R}}(\mathbf{X}, t)$ [mol/m^3] denote the total number of moles of mobile cations per unit volume of the reference body. Changes in ion concentration c_{R} in a part P of the reference body B are brought about by the migration of the species across its boundary $\partial\mathrm{P}$. The migration is characterized by a referential mass flux $\mathbf{j}_{\mathrm{R}}(\mathbf{X}, t)$, measured as the number of moles of the species per unit area per unit time, so that

$$-\int_{\partial\mathrm{P}} \mathbf{j}_{\mathrm{R}} \cdot \mathbf{n}_{\mathrm{R}}\, da_{\mathrm{R}}$$

represents the number of moles of cations entering P across $\partial\mathrm{P}$ per unit time.

[6] We do not treat electrostatic forces as body forces.

Thus the rate of change of the number of cations in P (assuming no internal sources) is given by

$$\dot{\overline{\int_{\mathrm{P}} c_{\mathrm{R}}\, dv_{\mathrm{R}}}} = -\int_{\partial \mathrm{P}} \mathbf{j}_{\mathrm{R}} \cdot \mathbf{n}_{\mathrm{R}}\, da_{\mathrm{R}} \tag{2.9}$$

for every part P. Bringing the time derivative inside the integral, and using the divergence theorem in (2.9) on the integral over ∂P, we find that

$$\int_{\mathrm{P}} (\dot{c}_{\mathrm{R}} + \mathrm{Div}\,\mathbf{j}_{\mathrm{R}})\, dv_{\mathrm{R}} = 0; \tag{2.10}$$

and since P is arbitrary, this leads to the following local balance law for referential cation concentration c_{R},

$$\dot{c}_{\mathrm{R}} = -\mathrm{Div}\,\mathbf{j}_{\mathrm{R}}\,. \tag{2.11}$$

This balance may also be expressed as balance in deformed body as,

$$\dot{c}_{\mathrm{R}} = -J\,\mathrm{div}\mathbf{j} \qquad \Longrightarrow \qquad \dot{\overline{(J\,c)}} = -J\,\mathrm{div}\mathbf{j} \qquad \Longrightarrow \qquad \dot{c} + c\,\mathrm{div}\mathbf{v} = -\mathrm{div}\mathbf{j}, \tag{2.12}$$

where $c = J^{-1}c_{\mathrm{R}}$ is the spatial concentration and $\mathbf{j} = J^{-1}\mathbf{F}\mathbf{j}_{\mathrm{R}}$ is the spatial flux of the cations.

2.3.2 Balance of charge

Initially, that is at time $t = 0$, the charge of the mobile univalent cations is

$$F\,\underbrace{c_{\mathrm{R}}^{+}(\mathbf{X}, 0)}_{\equiv c_{\mathrm{R}}(\mathbf{X},0)}, \tag{2.13}$$

and that of the fixed univalent anions is

$$-\,F\,c_{\mathrm{R}}^{-}(\mathbf{X}, 0), \tag{2.14}$$

measured in Coulombs per unit reference volume [C/m^3], where $F = 96,485$ C/mol is the Faraday constant. *Electroneutrality* at time $t = 0$ requires that,

$$F\,c_{\mathrm{R}}^{+}(\mathbf{X}, 0) - F\,c_{\mathrm{R}}^{-}(\mathbf{X}, 0) = 0\,, \tag{2.15}$$

or

$$c_{\mathrm{R}}^{+}(\mathbf{X}, 0) = c_{\mathrm{R}}^{-}(\mathbf{X}, 0) \equiv \underbrace{c_{\mathrm{R}0}}_{\text{fixed}}\,. \tag{2.16}$$

Then at time $t > 0$ the charge of the mobile cations is

$$F\,c_{\mathrm{R}}(\mathbf{X}, t), \tag{2.17}$$

and that of the fixed anions is

$$-\,F\,c_{\mathrm{R}0}. \tag{2.18}$$

Thus the *net charge* per unit reference volume of the body at times $t > 0$ is

$$q_{\mathrm{R}} = F\,(c_{\mathrm{R}} - c_{\mathrm{R}0}). \tag{2.19}$$

Let,

$$\mathbf{i}_{\mathrm{R}} \stackrel{\mathrm{def}}{=} F\mathbf{j}_{\mathrm{R}} \tag{2.20}$$

denote the referential *current density* or flux of positive charge due to the cations. Then the balance law (2.11) gives the following balance law for q_{R},

$$\dot{q}_{\mathrm{R}} = -\mathrm{Div}\,\mathbf{i}_{\mathrm{R}}. \tag{2.21}$$

2.4 Basic equations of electrostatics

The referential *electric field* in B is denoted by $\mathbf{e}_{\mathrm{R}}(\mathbf{X},t)$. In a polarizable material there is a vector field in B denoted by $\mathbf{d}_{\mathrm{R}}(\mathbf{X},t)$ called the *electric displacement*. In the theory formulated in this paper we only consider the *electrostatic* (quasi-static) limit as far as the electrical variables are concerned, so that time t only plays the role of a history parameter.

Under electrostatic conditions there are two governing Maxwell equations that must be satisfied. The first of these is *Faraday's law*, which in the electrostatic limit reads,

$$\operatorname{Curl}\mathbf{e}_{\mathrm{R}} = \mathbf{0}. \tag{2.22}$$

Satisfaction of (2.22) occurs automatically if we allow the electric field $\mathbf{e}_{\mathrm{R}}(\mathbf{X},t)$ to be represented as the gradient of an *electrostatic potential* $\phi(\mathbf{X},t)$,[7]

$$\mathbf{e}_{\mathrm{R}}(\mathbf{X},t) \stackrel{\mathrm{def}}{=} -\nabla\phi(\mathbf{X},t). \tag{2.23}$$

The negative sign in (2.23) follows the convention that the electric field points from a region of high potential to low potential, whereas the vector $\nabla\phi$ by definition points in the direction of increasing ϕ.

The second equation of electrostatics is given by *Gauss's law*. Gauss's law states that the divergence of the electric displacement $\mathbf{d}_{\mathrm{R}}$ must be equal to the density of the net charge per unit volume q_{R},

$$\operatorname{Div}\mathbf{d}_{\mathrm{R}} = q_{\mathrm{R}}\,. \tag{2.24}$$

Equations (2.22) and (2.24) constitute the governing equations for electrostatics in B. Using the conversion relations $\mathbf{e} = \mathbf{F}^{-\top}\mathbf{e}_{\mathrm{R}}$ and $\mathbf{d} = J^{-1}\mathbf{F}\mathbf{d}_{\mathrm{R}}$, the spatial counterparts of (2.22) and (2.24) are

$$\operatorname{curl}\mathbf{e} = \mathbf{0}, \tag{2.25}$$

and

$$\operatorname{div}\mathbf{d} = q \qquad \text{with} \qquad q = F\,(c - c_0)\,, \tag{2.26}$$

where

$$c = J^{-1}c_{\mathrm{R}}, \qquad c_0 = J^{-1}c_{\mathrm{R}0}\,. \tag{2.27}$$

are the concentration of the cations and anions per unit volume of the deformed body. Equations (2.25) and (2.26) constitute the governing equations for electrostatics in the deformed body $\mathcal{B}_t$.

2.5 Free-energy imbalance

Under isothermal conditions the two laws of thermodynamics reduce to the statement that *the rate of increase in free energy of any part* P *is less than or equal to the power expended on* P. Precisely, letting ψ_{R} denote the *free energy* per unit reference volume, this requirement takes the form of a free-energy imbalance

$$\overset{\cdot}{\int_{\mathrm{P}} \psi_{\mathrm{R}}\, dv_{\mathrm{R}}} \leq \mathcal{W}(\mathrm{P}) + \mathcal{E}(\mathrm{P}) + \mathcal{T}(\mathrm{P}), \tag{2.28}$$

where:

(i) The mechanical power $\mathcal{W}(\mathrm{P})$ exerted on P by the boundary tractions $\mathbf{T}_{\mathrm{R}}\mathbf{n}_{\mathrm{R}}$ and body force $\mathbf{b}_{\mathrm{R}}$ over the velocity $\dot{\boldsymbol{\chi}}$ is given by,

$$\mathcal{W}(\mathrm{P}) = \int_{\partial\mathrm{P}} (\mathbf{T}_{\mathrm{R}}\mathbf{n}_{\mathrm{R}})\cdot\dot{\boldsymbol{\chi}}\, da_{\mathrm{R}} + \int_{\mathrm{P}} \mathbf{b}_{\mathrm{R}}\cdot\dot{\boldsymbol{\chi}}\, dv_{\mathrm{R}}\,. \tag{2.29}$$

[7] Recall that for any scalar field ϕ, $\operatorname{Curl}(\nabla\phi) = \mathbf{0}$.

(ii) In electromagnetic field theory the electric power that is expended on P by charges external to P is characterized by an electromagnetic energy flux $\mathcal{E}(\mathrm{P})$ which in the electrostatic limit is given by (cf., e.g., Kovetz, 2000, § 54),

$$\mathcal{E}(\mathrm{P}) = -\int_{\partial \mathrm{P}} \phi\, \dot{\mathbf{d}}_{\mathrm{R}} \cdot \mathbf{n}_{\mathrm{R}}\, da_{\mathrm{R}} - \int_{\partial \mathrm{P}} \phi\, \mathbf{i}_{\mathrm{R}} \cdot \mathbf{n}_{\mathrm{R}}\, da_{\mathrm{R}}\,. \tag{2.30}$$

Using eq. (2.20) for the net current, (2.30) may be expressed as

$$\mathcal{E}(\mathrm{P}) = -\int_{\partial \mathrm{P}} \phi\, \dot{\mathbf{d}}_{\mathrm{R}} \cdot \mathbf{n}_{\mathrm{R}}\, da_{\mathrm{R}} - \int_{\partial \mathrm{P}} F\phi\, \mathbf{j}_{\mathrm{R}} \cdot \mathbf{n}_{\mathrm{R}}\, da_{\mathrm{R}}. \tag{2.31}$$

(iii) Finally to characterize the chemical energy carried into part P by cation transport we introduce

$$\mathcal{T}(\mathrm{P}) = -\int_{\partial \mathrm{P}} \mu\, \mathbf{j}_{\mathrm{R}} \cdot \mathbf{n}_{\mathrm{R}}\, da_{\mathrm{R}}, \tag{2.32}$$

with μ the *chemical potential* of the diffusing species (cf., e.g., Gurtin et al., 2010, § 65).

Thus, using (2.29), (2.31), and (2.32), the free energy imbalance (2.28) becomes

$$\dot{\overline{\int_{\mathrm{P}} \psi\, dv_{\mathrm{R}}}} \leq \int_{\partial \mathrm{P}} (\mathbf{T}_{\mathrm{R}} \mathbf{n}_{\mathrm{R}}) \cdot \dot{\boldsymbol{\chi}}\, da_{\mathrm{R}} + \int_{\mathrm{P}} \mathbf{b}_{\mathrm{R}} \cdot \dot{\boldsymbol{\chi}}\, dv_{\mathrm{R}} - \int_{\partial \mathrm{P}} \phi\, \dot{\mathbf{d}}_{\mathrm{R}} \cdot \mathbf{n}_{\mathrm{R}}\, da_{\mathrm{R}} - \int_{\partial \mathrm{P}} \omega \mathbf{j}_{\mathrm{R}} \cdot \mathbf{n}_{\mathrm{R}}\, da_{\mathrm{R}}\,, \tag{2.33}$$

where we have introduced the notation

$$\omega \stackrel{\mathrm{def}}{=} \mu + F\phi\,, \tag{2.34}$$

for an *electrochemical potential* of the cations.

Using the divergence theorem on the terms involving the integral over ∂P, (2.23), and the species balance (2.11) we obtain,

$$\left.\begin{aligned}
\int_{\partial \mathrm{P}} (\mathbf{T}_{\mathrm{R}} \mathbf{n}_{\mathrm{R}}) \cdot \dot{\boldsymbol{\chi}}\, da_{\mathrm{R}} &= \int_{\mathrm{P}} (\mathrm{Div}\, \mathbf{T}_{\mathrm{R}}) \cdot \dot{\boldsymbol{\chi}}\, dv + \int_{\mathrm{P}} \mathbf{T}_{\mathrm{R}} : \dot{\mathbf{F}} dv_{\mathrm{R}}, \\
-\int_{\partial \mathrm{P}} (\phi\, \dot{\mathbf{d}}_{\mathrm{R}}) \cdot \mathbf{n}_{\mathrm{R}}\, da_{\mathrm{R}} &= -\int_{\mathrm{P}} \phi\, (\mathrm{Div}\, \dot{\mathbf{d}}_{\mathrm{R}}) dv_{\mathrm{R}} - \int_{\mathrm{P}} (\nabla \phi) \cdot \dot{\mathbf{d}}_{\mathrm{R}}\, dv_{\mathrm{R}} \\
&= -\int_{\mathrm{P}} \phi\, (\mathrm{Div}\, \dot{\mathbf{d}}_{\mathrm{R}}) dv_{\mathrm{R}} + \int_{\mathrm{P}} \mathbf{e}_{\mathrm{R}} \cdot \dot{\mathbf{d}}_{\mathrm{R}}\, dv_{\mathrm{R}}\,, \\
-\int_{\partial \mathrm{P}} \omega\, \mathbf{j}_{\mathrm{R}} \cdot \mathbf{n}_{\mathrm{R}}\, da_{\mathrm{R}} &= -\left[\int_{\mathrm{P}} \omega\, \mathrm{Div}\, \mathbf{j}_{\mathrm{R}}\, dv_{\mathrm{R}} + \int_{\mathrm{P}} \mathbf{j}_{\mathrm{R}} \cdot \nabla \omega\, dv_{\mathrm{R}} \right] \\
&= \int_{\mathrm{P}} \Big(\omega \dot{c}_{\mathrm{R}} - \mathbf{j}_{\mathrm{R}} \cdot \nabla \omega \Big) dv_{\mathrm{R}}.
\end{aligned}\right\} \tag{2.35}$$

Substituting (2.35) in (2.33), and using (2.4), (2.34), and the rate form of (2.24) we obtain,

$$\int_{\mathrm{P}} \Big(\dot{\psi}_{\mathrm{R}} - \mathbf{T}_{\mathrm{R}} : \dot{\mathbf{F}} - \mu \dot{c}_{\mathrm{R}} - \mathbf{e}_{\mathrm{R}} \cdot \dot{\mathbf{d}}_{\mathrm{R}} + \mathbf{j}_{\mathrm{R}} \cdot \nabla \omega \Big)\, dv_{\mathrm{R}} \leq 0. \tag{2.36}$$

Since (2.36) has to hold for all parts P, we obtain a local free-energy imbalance in the form,

$$\dot{\psi}_{\mathrm{R}} - \mathbf{T}_{\mathrm{R}} : \dot{\mathbf{F}} - \mu \dot{c}_{\mathrm{R}} - \mathbf{e}_{\mathrm{R}} \cdot \dot{\mathbf{d}}_{\mathrm{R}} + \mathbf{j}_{\mathrm{R}} \cdot \nabla \omega \leq 0. \tag{2.37}$$

For later use we define the dissipation density $\mathcal{D} \geq 0$ per unit volume per unit time by

$$\mathcal{D} = \mathbf{T}_{\mathrm{R}} : \dot{\mathbf{F}} + \mu \dot{c}_{\mathrm{R}} + \mathbf{e}_{\mathrm{R}} \cdot \dot{\mathbf{d}}_{\mathrm{R}} - \mathbf{j}_{\mathrm{R}} \cdot \nabla \omega - \dot{\psi}_{\mathrm{R}} \geq 0. \tag{2.38}$$

2.6 The decomposition $\mathbf{F} = \mathbf{F}^e\mathbf{F}^s$

Next, to account for coupling between diffusion of the cations and mechanical swelling, we base our theory on a multiplicative decomposition of the deformation gradient (Chester and Anand, 2010)

$$\mathbf{F} = \mathbf{F}^e\mathbf{F}^s, \tag{2.39}$$

where,

- $\mathbf{F}^s$ represents the local distortion of the material neighborhood of $\mathbf{X}$ due to the insertion/extraction of migrating cations and the associated volume changes, and
- $\mathbf{F}^e$ represents the subsequent stretching and rotation of this coherent species-distorted material neighborhood, and thereby represents a corresponding elastic mechanical distortion.

We refer to $\mathbf{F}^s$ and $\mathbf{F}^e$ as the swelling and mechanical distortions, respectively. Hence we have

$$J = J^eJ^s, \quad \text{and we assume that} \quad J^e = \det \mathbf{F}^e > 0, \quad \text{and} \quad J^s = \det \mathbf{F}^s > 0, \tag{2.40}$$

so that $\mathbf{F}^e$ and $\mathbf{F}^s$ are invertible.

The total and elastic right Cauchy-Green deformation tensors are given by

$$\mathbf{C} = \mathbf{F}^\top\mathbf{F} \qquad \text{and} \qquad \mathbf{C}^e = \mathbf{F}^{e\top}\mathbf{F}^e, \tag{2.41}$$

respectively. Further, by the definition $(2.1)_3$, we have

$$\mathbf{L} = \mathbf{L}^e + \mathbf{F}^e\mathbf{L}^s\mathbf{F}^{e-1}, \quad \text{with} \quad \mathbf{L}^e = \dot{\mathbf{F}}^e\mathbf{F}^{e-1}, \quad \text{and} \quad \mathbf{L}^s = \dot{\mathbf{F}}^s\mathbf{F}^{s-1}, \tag{2.42}$$

where $\mathbf{L}^s$ represents a distortion rate due to insertion/extraction of the migrating cations.

Finally, we assume that the swelling distortion $\mathbf{F}^s$ is isotropic and given by,

$$\mathbf{F}^s = \lambda^s\mathbf{1}, \quad \lambda^s = (J^s)^{1/3} > 0; \tag{2.43}$$

we call λ^s the swell-stretch. Further, from the definition of $\mathbf{L}^s$ in (2.42), and the specific expression for $\mathbf{F}^s$ in (2.43), we have,

$$\mathbf{L}^s = (\dot{\lambda}^s\lambda^{s-1})\mathbf{1}; \tag{2.44}$$

and since $\dot{J}^s = J^s\mathrm{tr}\mathbf{L}^s$, we have

$$\mathbf{L}^s = \frac{1}{3}(\dot{J}^sJ^{s-1})\mathbf{1}. \tag{2.45}$$

2.7 Constitutive constraint between J^s and c_{R}

Now, $(J^s - 1)$ represents the change in volume per unit reference volume due to swelling caused by the migrating cations. We assume that this change arises entirely due to the change in the concentration of the hydrated cations, so that we have the important swelling constraint,

$$J^s = 1 + \Omega(c_{\mathrm{R}} - c_{\mathrm{R}0}), \tag{2.46}$$

where

- Ω is the molar volume of the mobile hydrated cations,

and $c_{\mathrm{R}0}$ is the initial concentration of the cations which is equal to that of the fixed anions. Thus note that,

$$\dot{J}^s = \Omega\dot{c}_{\mathrm{R}}. \tag{2.47}$$

2.8 Free-energy imbalance revisted

Next, using (2.39), $(2.42)_2$, and (2.6), we may write the stress power $\mathbf{T}_{\mathrm{R}} : \dot{\mathbf{F}}$ appearing in the free-energy imbalance (2.37) as

$$\mathbf{T}_{\mathrm{R}} : \dot{\mathbf{F}} = J^s \tfrac{1}{2} (J^e \mathbf{F}^{e\,-1} \mathbf{T} \mathbf{F}^{e-\top}) : \dot{\mathbf{C}}^e + J^s (J^e \mathbf{F}^{e\top} \mathbf{T} \mathbf{F}^{e-\top}) : \mathbf{L}^s.$$

For convenience, we define two new stress measures

$$\mathbf{T}^e \stackrel{\text{def}}{=} J^e \mathbf{F}^{e\,-1} \mathbf{T} \mathbf{F}^{e\,-\top} \qquad \text{and} \qquad \mathbf{M}^e \stackrel{\text{def}}{=} \mathbf{C}^e \mathbf{T}^e = J^e \mathbf{F}^{e\top} \mathbf{T} \mathbf{F}^{e-\top}, \tag{2.48}$$

which we call the *elastic second Piola stress* and the *Mandel stress*, respectively. Then

$$\mathbf{T}_{\mathrm{R}} : \dot{\mathbf{F}} = J^s \tfrac{1}{2} \mathbf{T}^e : \dot{\mathbf{C}}^e + J^s \mathbf{M}^e : \mathbf{L}^s \,. \tag{2.49}$$

Further, recalling (2.45) we may write (2.49) as

$$\mathbf{T}_{\mathrm{R}} : \dot{\mathbf{F}} = J^s \tfrac{1}{2} \mathbf{T}^e : \dot{\mathbf{C}}^e + \frac{1}{3} (\operatorname{tr} \mathbf{M}^e) \dot{J}^s. \tag{2.50}$$

Let

$$p \stackrel{\text{def}}{=} -\frac{1}{3} (\operatorname{tr} \mathbf{M}^e) = J^e \left(-\frac{1}{3} \operatorname{tr} \mathbf{T} \right), \tag{2.51}$$

define a *mean normal pressure*. Then, using (2.51) and (2.47), the stress-power (2.50) may be written as

$$\mathbf{T}_{\mathrm{R}} : \dot{\mathbf{F}} = \tfrac{1}{2} \, J^s \, \mathbf{T}^e : \dot{\mathbf{C}}^e - p \, \Omega \, \dot{c}_{\mathrm{R}}. \tag{2.52}$$

Introducing a net chemical potential defined by

$$\mu_{\text{net}} \stackrel{\text{def}}{=} \mu - p \, \Omega, \tag{2.53}$$

we may rewrite the free-energy imbalance (2.37) under isothermal conditions as

$$\dot{\psi}_{\mathrm{R}} - \tfrac{1}{2} \, J^s \, \mathbf{T}^e : \dot{\mathbf{C}}^e - \mu_{\text{net}} \dot{c}_{\mathrm{R}} - \mathbf{e}_{\mathrm{R}} \cdot \dot{\mathbf{d}}_{\mathrm{R}} + \mathbf{j}_{\mathrm{R}} \cdot \nabla \omega \leq 0. \tag{2.54}$$

Also the dissipation density (2.38) becomes

$$\mathcal{D} = \tfrac{1}{2} \, J^s \, \mathbf{T}^e : \dot{\mathbf{C}}^e + \mu_{\text{net}} \dot{c}_{\mathrm{R}} + \mathbf{e}_{\mathrm{R}} \cdot \dot{\mathbf{d}}_{\mathrm{R}} - \mathbf{j}_{\mathrm{R}} \cdot \nabla \omega - \dot{\psi}_{\mathrm{R}} \geq 0. \tag{2.55}$$

Remark. For brevity we have not discussed the transformation properties under a change in frame of the various fields appearing in our theory. Here, we simply note that all quantities in the free energy imbalance (2.54) are invariant under a change in frame (Gurtin et al., 2010).

2.9 Constitutive theory

Let $\mathbf{\Lambda}$ represent the list

$$\mathbf{\Lambda} = \{ \mathbf{C}^e, c_{\mathrm{R}}, \mathbf{d}_{\mathrm{R}} \} \,. \tag{2.56}$$

Guided by the free energy imbalance (2.54), we begin by assuming constitutive equations for the free energy ψ_{R}, the stress $\mathbf{T}^e$, the net chemical potential μ_{net}, and the electric field $\mathbf{e}_{\mathrm{R}}$ of the form

$$\psi_{\mathrm{R}} = \hat{\psi}_{\mathrm{R}}(\mathbf{\Lambda}), \qquad \mathbf{T}^e = \hat{\mathbf{T}}^e(\mathbf{\Lambda}), \qquad \mu_{\text{net}} = \hat{\mu}_{\text{net}}(\mathbf{\Lambda}), \quad \mathbf{e}_{\mathrm{R}} = \hat{\mathbf{e}}_{\mathrm{R}}(\mathbf{\Lambda}). \tag{2.57}$$

Then,

$$\dot{\psi}_{\mathrm{R}} = \frac{\partial \hat{\psi}_{\mathrm{R}}(\mathbf{\Lambda})}{\partial \mathbf{C}^e} : \dot{\mathbf{C}}^e + \frac{\partial \hat{\psi}_{\mathrm{R}}(\mathbf{\Lambda})}{\partial c_{\mathrm{R}}} \dot{c}_{\mathrm{R}} + \frac{\partial \hat{\psi}_{\mathrm{R}}(\mathbf{\Lambda})}{\partial \mathbf{d}_{\mathrm{R}}} \cdot \dot{\mathbf{d}}_{\mathrm{R}} \,. \tag{2.58}$$

Using (2.58) and substituting the constitutive equations (2.57) into the free-energy imbalance (2.54), we find that it may be written as

$$\left[\frac{\partial\hat{\psi}_{\rm R}(\mathbf{\Lambda})}{\partial\mathbf{C}^e}-\tfrac{1}{2}J^s\,\hat{\mathbf{T}}^e(\mathbf{\Lambda})\right]:\dot{\mathbf{C}}^e+\left[\frac{\partial\hat{\psi}_{\rm R}(\mathbf{\Lambda})}{\partial c_{\rm R}}-\hat{\mu}_{\rm net}(\mathbf{\Lambda})\right]\dot{c}_{\rm R}+\left[\frac{\partial\hat{\psi}_{\rm R}(\mathbf{\Lambda})}{\partial\mathbf{d}_{\rm R}}-\hat{\mathbf{e}}_{\rm R}(\mathbf{\Lambda})\right]\cdot\dot{\mathbf{d}}_{\rm R}+\mathbf{j}_{\rm R}\cdot\nabla\omega\leq 0. \quad (2.59)$$

We assume constitutively that the free-energy delivers the stress $\mathbf{T}^e$, the net chemical potential $\mu_{\rm net}$, and the electric field $\mathbf{e}_{\rm R}$ through the state relations

$$\mathbf{T}^e=J^{s-1}\left(2\frac{\partial\hat{\psi}_{\rm R}(\mathbf{\Lambda})}{\partial\mathbf{C}^e}\right),\qquad \mu_{\rm net}=\frac{\partial\hat{\psi}_{\rm R}(\mathbf{\Lambda})}{\partial c_{\rm R}},\qquad \mathbf{e}_{\rm R}=\frac{\partial\hat{\psi}_{\rm R}(\mathbf{\Lambda})}{\partial\mathbf{d}_{\rm R}}. \quad (2.60)$$

Using (2.60) in (2.59) leads to the following *dissipation inequality*

$$\mathcal{D}=-\mathbf{j}_{\rm R}\cdot\nabla\omega\geq 0. \quad (2.61)$$

2.10 Chemical potential and electrochemical potential

The thermodynamically-consistent constitutive equation $(2.60)_2$, together with the definition (2.53) of $\mu_{\rm net}$, gives that the *chemical potential* for the cations,

$$\mu=\frac{\partial\hat{\psi}_{\rm R}(\mathbf{\Lambda})}{\partial c_{\rm R}}+p\,\Omega\,. \quad (2.62)$$

and recalling (2.34) we have that the *electrochemical potential* ω is given by

$$\omega=\frac{\partial\hat{\psi}(\mathbf{\Lambda})}{\partial c_{\rm R}}+p\,\Omega+F\,\phi\,. \quad (2.63)$$

2.11 Dissipative constitutive equations

We assume that the flux $\mathbf{j}_{\rm R}$ depends *linearly* on the gradient $\nabla\omega$ of electrochemical potential gradient, by a *Fick*-type relation,

$$\mathbf{j}_{\rm R}=-\mathbf{M}(\mathbf{\Lambda})\nabla\omega, \quad (2.64)$$

with $\mathbf{M}$ the **mobility tensor**. A consequence of the species-transport inequality (2.61) is then that the mobility tensor $\mathbf{M}$ is positive-semidefinite,

$$\mathbf{p}\cdot\mathbf{M}(\mathbf{\Lambda})\mathbf{p}\geq 0\qquad\text{for all }\mathbf{p}\neq\mathbf{0}. \quad (2.65)$$

2.12 Specialization of the constitutive equations

The theory presented thus far is quite general. We now introduce special constitutive equations which should be useful in applications. We limit our attention to materials which may be idealized to be isotropic.

2.12.1 Free energy

Henceforth we restrict our attention to materials for which the response function $\hat{\psi}(\mathbf{\Lambda})$ may be taken in the separable form

$$\hat{\psi}_{\rm R}(\mathbf{C}^e,c_{\rm R},\mathbf{d}_{\rm R})=\hat{\psi}_{\rm R}^{(\rm mech)}(\mathbf{C}^e,c_{\rm R})+\hat{\psi}_{\rm R}^{(\rm es)}(\mathbf{C}^e,c_{\rm R},\mathbf{d}_{\rm R})+\hat{\psi}_{\rm R}^{(\rm mix)}(\mathbf{C}^e,c_{\rm R}). \quad (2.66)$$

Here:

(i) $\hat{\psi}_{\rm R}^{(\rm mech)}(\mathbf{C}^e,c_{\rm R})$ is a contribution to the change in the free energy due to the elastic deformation of the host material, which is taken to be an isotropic function of $\mathbf{C}^e$. An immediate consequence is that this free energy function has the representation

$$\hat{\psi}^{(\rm mech)}(\mathbf{C}^e,c_{\rm R})=\tilde{\psi}_{\rm R}^{(\rm mech)}(\mathcal{I}_{\mathbf{C}^e},c_{\rm R}), \quad (2.67)$$

with

$$\mathcal{I}_{\mathbf{C}^e} = \Big(I_1(\mathbf{C}^e), I_2(\mathbf{C}^e), I_3(\mathbf{C}^e)\Big)$$

the list of principal invariants of $\mathbf{C}^e$. Thus, from $(2.60)_1$, it follows that the mechanical contribution to the elastic second Piola stress $\mathbf{T}^e$ is

$$\mathbf{T}^{e\,(\mathrm{mech})} = J^{s-1}\Big(2\,\frac{\partial\tilde{\psi}^{(\mathrm{mech})}(\mathcal{I}_{\mathbf{C}^e}, c_{\mathrm{R}})}{\partial\mathbf{C}^e}\Big), \tag{2.68}$$

and that $\mathbf{T}^{e\,(\mathrm{mech})}$ is an *isotropic function of* $\mathbf{C}^e$. Then since the Mandel stress is defined by $(2.48)_2$, the mechanical contribution to the Mandel stress is

$$\mathbf{M}^{e\,(\mathrm{mech})} = \mathbf{C}^e\mathbf{T}^{e\,(\mathrm{mech})}, \tag{2.69}$$

we find that $\mathbf{T}^{e\,(\mathrm{mech})}$ and $\mathbf{C}^e$ commute,

$$\mathbf{C}^e\mathbf{T}^{e\,(\mathrm{mech})} = \mathbf{T}^{e\,(\mathrm{mech})}\mathbf{C}^e, \tag{2.70}$$

and hence that the mechanical Mandel stress $\mathbf{M}^{e\,(\mathrm{mech})}$ is symmetric. Next, the spectral representation of $\mathbf{C}^e$ is

$$\mathbf{C}^e = \sum_{i=1}^{3} \lambda_i^{e\,2}\mathbf{r}_i^e \otimes \mathbf{r}_i^e, \tag{2.71}$$

where $(\mathbf{r}_1^e, \mathbf{r}_2^e, \mathbf{r}_2^e)$ are the orthonormal eigenvectors of $\mathbf{C}^e$ and $\mathbf{U}^e$, and $(\lambda_1^e, \lambda_2^e, \lambda_3^e)$ are the positive eigenvalues of $\mathbf{U}^e$. Instead of using the invariants $\mathcal{I}_{\mathbf{C}^e}$, this free energy may be alternatively expressed in terms of the principal stretches and species concentration as

$$\hat{\psi}_{\mathrm{R}}^{(\mathrm{mech})}(\mathbf{C}^e, c_{\mathrm{R}}) = \check{\psi}_{\mathrm{R}}^{(\mathrm{mech})}(\lambda_1^e, \lambda_2^e, \lambda_3^e, c_{\mathrm{R}}). \tag{2.72}$$

Let

$$\mathbf{E}^e \stackrel{\mathrm{def}}{=} \ln \mathbf{U}^e = \sum_{i=1}^{3} E_i^e\, \mathbf{r}_i^e \otimes \mathbf{r}_i^e, \tag{2.73}$$

denote the logarithmic elastic strain with principal values

$$E_i^e \stackrel{\mathrm{def}}{=} \ln \lambda_i^e\,, \tag{2.74}$$

and consider an elastic free energy function of the form

$$\check{\psi}_{\mathrm{R}}^{(\mathrm{mech})}(\lambda_1^e, \lambda_2^e, \lambda_3^e, c_{\mathrm{R}}) = \check{\psi}_{\mathrm{R}}^{(\mathrm{mech})}(E_1^e, E_2^e, E_3^e, c_{\mathrm{R}}). \tag{2.75}$$

Then, straightforward calculations show that the Mandel stress is given by

$$\mathbf{M}^{e\,(\mathrm{mech})} = J^{s-1}\sum_{i=1}^{3}\, \frac{\partial\check{\psi}(E_1^e, E_2^e, E_3^e, c_{\mathrm{R}})}{\partial E_i^e}\, \mathbf{r}_i^e \otimes \mathbf{r}_i^e. \tag{2.76}$$

With the logarithmic elastic strain defined by (2.73), and bearing in mind (2.75) and (2.76), for isotropic elastic materials we henceforth consider a free energy of the form

$$\psi_{\mathrm{R}}^{(\mathrm{mech})}(\mathbf{C}^e, c_{\mathrm{R}}) = \bar{\psi}_{\mathrm{R}}(\mathcal{I}_{\mathbf{E}^e}, c_{\mathrm{R}}) \tag{2.77}$$

with $\mathcal{I}_{\mathbf{E}^e}$ a list of principal invariants of $\mathbf{E}^e$, or equivalently a list of principal values of $\mathbf{E}^e$. The Mandel stress is then given by

$$\mathbf{M}^{e\,(\mathrm{mech})} = J^{s-1}\left(\frac{\partial\bar{\psi}_{\mathrm{R}}^{(\mathrm{mech})}(\mathcal{I}_{\mathbf{E}^e}, c_{\mathrm{R}})}{\partial\mathbf{E}^e}\right), \tag{2.78}$$

and the corresponding mechanical contribution to the Cauchy stress is

$$\mathbf{T}^{(\mathrm{mech})} = J^{e-1}\mathbf{R}^e\mathbf{M}^{e\,(\mathrm{mech})}\mathbf{R}^{e\top} = J^{-1}\mathbf{R}^e\left(\frac{\partial\bar{\psi}_{\mathrm{R}}^{(\mathrm{mech})}(\mathcal{I}_{\mathbf{E}^e}, c_{\mathrm{R}})}{\partial\mathbf{E}^e}\right)\mathbf{R}^{e\top}, \tag{2.79}$$

and the Piola stress by

$$\mathbf{T}_{\mathrm{R}}^{(\mathrm{mech})} \stackrel{\mathrm{def}}{=} \Big(\mathbf{R}^e \frac{\partial \bar{\psi}_{\mathrm{R}}^{(\mathrm{mech})}(\mathcal{I}_{\mathbf{E}^e}, c_{\mathrm{R}})}{\partial \mathbf{E}^e}\, \mathbf{R}^{e\top}\Big)\mathbf{F}^{-\top}. \tag{2.80}$$

Next, as a simple specific form for $\bar{\psi}_{\mathrm{R}}^{(\mathrm{mech})}(\mathcal{I}_{\mathbf{E}^e}, c_{\mathrm{R}})$ we take it to given by[8]

$$\bar{\psi}_{\mathrm{R}}^{(\mathrm{mech})}(\mathcal{I}_{\mathbf{E}^e}, c_{\mathrm{R}}) = J^s\Big[\tfrac{1}{2}\mathbf{E}^e : \mathbb{C}[\mathbf{E}^e]\Big], \qquad \mathbb{C} \stackrel{\mathrm{def}}{=} 2G\mathbb{I}^{\mathrm{sym}} + \big(K - \tfrac{2}{3}G\big)\mathbf{1}\otimes\mathbf{1}, \tag{2.81}$$

where $\mathbb{C}$ is the elasticity tensor, with $\mathbb{I}^{\mathrm{sym}}$ and $\mathbf{1}$ the symmetric fourth- and second-order identity tensors, and the parameters

$$G > 0, \qquad K > 0, \tag{2.82}$$

are shear modulus and bulk modulus, respectively.[9] the *concentration-independent* shear modulus and bulk modulus, respectively. The term

$$\tfrac{1}{2}\mathbf{E}^e : \mathbb{C}[\mathbf{E}^e]$$

in (2.81) is a measure of the free energy per unit volume of the intermediate space defined by the range of $\mathbf{F}^s(\mathbf{X})$, and multiplication of this term by J^s gives us the free energy per unit volume of the reference space.

(ii) $\hat{\psi}_{\mathrm{R}}^{(\mathrm{es})}(\mathbf{C}^e, c_{\mathrm{R}}, \mathbf{d}_{\mathrm{R}})$ is an electrostatic or polarization energy. We consider a special form for this energy (Suo, 2010),

$$\psi_{\mathrm{R}}^{(\mathrm{es})} = J\left(\frac{1}{2\varepsilon}\mathbf{d}\cdot\mathbf{d}\right), \tag{2.83}$$

which is *isotropic in the deformed body*, with $\varepsilon > 0$ a scalar constant representing the *effective electrical permittivity* of the material, which in general could depend on the cation concentration, but we take it to be a constant here. Since $\mathbf{d} = J^{-1}\mathbf{F}\mathbf{d}_{\mathrm{R}}$, we may express this free energy as

$$\psi_{\mathrm{R}}^{(\mathrm{es})} = J^{-1}\left(\frac{1}{2\varepsilon}\mathbf{d}_{\mathrm{R}}\cdot\mathbf{C}\mathbf{d}_{\mathrm{R}}\right). \tag{2.84}$$

The effective electrical permittivity ε is often expressed as

$$\varepsilon = \varepsilon_r\, \varepsilon_0\,, \tag{2.85}$$

where $\varepsilon_0 = 8.85\times 10^{-12}\,\mathrm{F/m}$ is a scalar representing the electrical permittivity of vacuum, and ε_r is a *relative electrical permittivity* of the material.

(iii) $\hat{\psi}_{\mathrm{R}}^{(\mathrm{mix})}(\mathbf{C}^e, c_{\mathrm{R}})$ is the change in free energy due to mixing of the migrating cations in the host material. As a simple continuum approximation of this mixing energy we take it to be given by a concentrated solution model of the form

$$\psi_{\mathrm{R}}^{(\mathrm{mix})}(c_{\mathrm{R}}) = \mu_0 c_{\mathrm{R}} + (R\vartheta\, c_{\mathrm{R}}^{\max})\left[\bar{c}\ln\bar{c} + (1-\bar{c})\ln(1-\bar{c})\right], \tag{2.86}$$

where

$$\bar{c} \stackrel{\mathrm{def}}{=} \frac{c_{\mathrm{R}}}{c_{\mathrm{R}}^{\max}}, \qquad 0 \le \bar{c} \le 1,$$

is a normalized species concentration, with $c_{\mathrm{R}}^{\max}$ the concentration of the species in moles per unit reference volume when all the accommodating sites in the host material are filled. Also R is the universal gas constant, and ϑ is the absolute temperature, assumed to be constant in our isothermal theory.

Thus, using (2.81), (2.84), and (2.86) in (2.66), a simple form of the free energy function which accounts for the combined effects of finite elastic stretching, electrostatic interactions, mixing and swelling, is

$$\psi_{\mathrm{R}} = J^s\Big(\tfrac{1}{2}\mathbf{E}^e : \mathbb{C}[\mathbf{E}^e]\Big) + J^{-1}\left(\frac{1}{2\varepsilon}\mathbf{d}_{\mathrm{R}}\cdot\mathbf{C}\mathbf{d}_{\mathrm{R}}\right) + \mu_0 c_{\mathrm{R}} + (R\vartheta\, c_{\mathrm{R}}^{\max})\left[\bar{c}\ln\bar{c} + (1-\bar{c})\ln(1-\bar{c})\right]. \tag{2.87}$$

[8]This is a simple generalization of the classical strain energy function of infinitesimal isotropic elasticity to moderately large stretches using the logarithmic elastic strain (Anand, 1979).

[9]In general, the elastic constants can depend on the cation concentration, but not much is known about this dependence, so for simplicity we take it to be a constant.

2.12.2 Electric field

From $(2.60)_3$ and (2.87) the referential electric field is given by

$$\mathbf{e}_{\mathrm{R}} = \frac{1}{\varepsilon}\, J^{-1}\, \mathbf{C}\mathbf{d}_{\mathrm{R}}. \tag{2.88}$$

Thus,

$$\mathbf{d}_{\mathrm{R}} = \varepsilon\, J\mathbf{C}^{-1}\mathbf{e}_{\mathrm{R}}. \tag{2.89}$$

Further, using the conversion relations $\mathbf{e} = \mathbf{F}^{-\top}\mathbf{e}_{\mathrm{R}}$ and $\mathbf{d} = J^{-1}\mathbf{F}\mathbf{d}_{\mathrm{R}}$, we obtain that the spatial electric flux density is given by

$$\mathbf{d} = \varepsilon\mathbf{e}. \tag{2.90}$$

2.12.3 Strain decomposition

From (2.39) and (2.43) we have that,

$$\mathbf{F} = \mathbf{F}^e\mathbf{F}^s = \lambda^s\mathbf{F}^e, \tag{2.91}$$

with the polar decompositions of $\mathbf{F}$ and $\mathbf{F}^e$ given by

$$\mathbf{F} = \mathbf{R}\mathbf{U} \qquad \text{and} \qquad \mathbf{F}^e = \mathbf{R}^e\mathbf{U}^e, \tag{2.92}$$

where $\mathbf{R}$ and $\mathbf{U}$ are the orthogonal rotation and right stretch tensors respectively and $\mathbf{R}^e$ and $\mathbf{U}^e$ are the elastic rotation and right elastic stretch tensors. Thus,

$$\mathbf{R}\mathbf{U} = \lambda^s\mathbf{R}^e\mathbf{U}^e. \tag{2.93}$$

By the uniqueness of the polar decomposition we have,

$$\mathbf{R} = \mathbf{R}^e \quad \text{and} \qquad \mathbf{U} = \lambda^s\mathbf{U}^e. \tag{2.94}$$

Then, defining the total logarithmic strain measure as

$$\mathbf{E} \stackrel{\text{def}}{=} \ln\mathbf{U}, \tag{2.95}$$

we obtain, using (2.43) and (2.46), that the total logarithmic strain may be decomposed as the sum of an elastic strain and a chemical swelling strain,

$$\begin{aligned}\mathbf{E} &= \mathbf{E}^e + \ln\lambda^s\mathbf{1}\\ &= \underbrace{\mathbf{E}^e}_{\text{elastic strain}} + \underbrace{\frac{1}{3}\ln(1+\Omega(c_{\mathrm{R}}-c_{\mathrm{R}0}))\mathbf{1}}_{\text{chemical strain}}.\end{aligned} \tag{2.96}$$

2.12.4 Stress

Mechanical contribution to the stress

From (2.78) and (2.87), the mechanical contribution to the Mandel stress is

$$\mathbf{M}^{e\,(\mathrm{mech})} = 2G\mathbf{E}^e + (K-(2/3)G)(\operatorname{tr}\mathbf{E}^e)\mathbf{1}. \tag{2.97}$$

Then, using (2.79) we find that the mechanical contribution to the Cauchy stress r is given by

$$\mathbf{T}^{(\mathrm{mech})} = J^{e-1}\left[2G\mathbf{E}^e_{\mathrm{H}} + (K-(2/3)G)(\operatorname{tr}\mathbf{E}^e_{\mathrm{H}})\mathbf{1}\right]. \tag{2.98}$$

Hence the mechanical contribution to the Piola stress, $\mathbf{T}^{(\mathrm{mech})}_{\mathrm{R}} = J\mathbf{T}^{(\mathrm{mech})}\mathbf{F}^{-\top}$, is given by

$$\mathbf{T}^{(\mathrm{mech})}_{\mathrm{R}} = J^s\left[2G\mathbf{E}^e_{\mathrm{H}} + (K-(2/3)G)(\operatorname{tr}\mathbf{E}^e_{\mathrm{H}})\mathbf{1}\right]\mathbf{F}^{-\top}. \tag{2.99}$$

In (2.98) and (2.99) we have used the notation

$$\mathbf{E}^e_{\text{H}} \stackrel{\text{def}}{=} \ln \mathbf{V}^e \tag{2.100}$$

for the logarithmic elastic strain in the deformed body. Recalling (2.96), we can similarly decompose the spatial Hencky strain into elastic and chemical parts, viz.

$$\mathbf{E}_{\text{H}} = \mathbf{E}^e_{\text{H}} + \frac{1}{3}\ln\left[1+\Omega(c_{\text{R}}-c_{\text{R}0})\right]\mathbf{1} \qquad \text{where } \mathbf{E}_{\text{H}} = \ln \mathbf{V},$$

and hence write (2.98) as,

$$\mathbf{T}^{(\text{mech})} = J^{e-1}\Big[2G\mathbf{E}_{\text{H}} + (K-(2/3)G)(\operatorname{tr}\mathbf{E}_{\text{H}})\mathbf{1} - K\ln\left[1+\Omega(c_{\text{R}}-c_{\text{R}0})\right]\mathbf{1}\Big]. \tag{2.101}$$

Electrostatic contribution to the stress

Since

$$J^{-1} = J^{e-1}J^{s-1} = J^{e-1}(\lambda^s)^{-3} \qquad \text{and} \qquad \mathbf{C} = (\lambda^s)^2\mathbf{C}^e,$$

we may rewrite (2.84) as

$$\psi^{(\text{es})}_{\text{R}} = \frac{(\lambda^s)^{-1}}{2\varepsilon}J^{e-1}\left(\mathbf{d}_{\text{R}}\cdot\mathbf{C}^e\mathbf{d}_{\text{R}}\right), \tag{2.102}$$

From $(2.60)_1$ and (2.102) the electrostatic contribution to the elastic second Piola stress is

$$\mathbf{T}^{e\,(\text{es})} = J^{s-1}\left(2\frac{(\lambda^s)^{-1}}{2\varepsilon}\left[\frac{\partial J^{e-1}}{\partial\mathbf{C}^e}\left(\mathbf{d}_{\text{R}}\cdot\mathbf{C}^e\mathbf{d}_{\text{R}}\right) + J^{e-1}\frac{\partial}{\partial\mathbf{C}^e}\left(\mathbf{d}_{\text{R}}\cdot\mathbf{C}^e\mathbf{d}_{\text{R}}\right)\right]\right).$$

Using,

$$\frac{\partial J^{e-1}}{\partial\mathbf{C}^e} = -\tfrac{1}{2}J^{e-1}\mathbf{C}^{e-1}. \tag{2.103}$$

and

$$\frac{\partial}{\partial\mathbf{C}^e}\left(\mathbf{d}_{\text{R}}\cdot\mathbf{C}^e\mathbf{d}_{\text{R}}\right) = \mathbf{d}_{\text{R}}\otimes\mathbf{d}_{\text{R}}. \tag{2.104}$$

we obtain

$$\mathbf{T}^{e\,(\text{es})} = J^{-1}(\lambda^s)^{-1}\left(\frac{1}{\varepsilon}\left[\mathbf{d}_{\text{R}}\otimes\mathbf{d}_{\text{R}} - \tfrac{1}{2}\mathbf{C}^{e-1}\left(\mathbf{d}_{\text{R}}\cdot\mathbf{C}^e\mathbf{d}_{\text{R}}\right)\right]\right). \tag{2.105}$$

Hence the electrostatic contribution to the Cauchy stress, $\mathbf{T}^{(\text{pol})} = J^{e-1}\mathbf{F}^e\mathbf{T}^{e\,(\text{pol})}\mathbf{F}^{e\top}$, after a bit of algebra is,

$$\mathbf{T}^{(\text{es})} = \varepsilon\left[\mathbf{e}\otimes\mathbf{e} - \tfrac{1}{2}(\mathbf{e}\cdot\mathbf{e})\mathbf{1}\right], \tag{2.106}$$

which is the usual form of the Maxwell stress.

Total stress

Using (2.101) and (2.106), the total Cauchy stress is then given by,

$$\boxed{\mathbf{T} = \underbrace{J^{e-1}\Big[2G\mathbf{E}_{\text{H}} + (K-(2/3)G)(\operatorname{tr}\mathbf{E}_{\text{H}})\mathbf{1} - K\ln\left[1+\Omega(c_{\text{R}}-c_{\text{R}0})\right]\mathbf{1}\Big]}_{\text{chemo-mechanical stress}} + \underbrace{\varepsilon\left[\mathbf{e}\otimes\mathbf{e} - \tfrac{1}{2}\left(\mathbf{e}\cdot\mathbf{e}\right)\mathbf{1}\right]}_{\text{Maxwell stress}},} \tag{2.107}$$

and since $\mathbf{T}_{\text{R}} = J\mathbf{T}\mathbf{F}^{-\top}$, the total Piola stress is

$$\boxed{\mathbf{T}_{\text{R}} = \underbrace{J^{s}\Big[2G\mathbf{E}_{\text{H}} + (K-(2/3)G)(\operatorname{tr}\mathbf{E}_{\text{H}})\mathbf{1} - K\ln\left[1+\Omega(c_{\text{R}}-c_{\text{R}0})\right]\mathbf{1}\Big]\mathbf{F}^{-\top}}_{\text{chemo-mechanical stress}} + \underbrace{\varepsilon J\left[\mathbf{e}\otimes\mathbf{e} - \tfrac{1}{2}\left(\mathbf{e}\cdot\mathbf{e}\right)\mathbf{1}\right]\mathbf{F}^{-\top}}_{\text{Maxwell stress}}.} \tag{2.108}$$

2.12.5 Electrochemical potential

Aside: Recall,

$$\psi_{\mathrm{R}} = J^s\left(\tfrac{1}{2}\mathbf{E}^e : \mathbb{C}[\mathbf{E}^e]\right) + J^{-1}\left(\frac{1}{2\varepsilon}\mathbf{d}_{\mathrm{R}}\cdot\mathbf{C}\mathbf{d}_{\mathrm{R}}\right) + \mu_0 c_{\mathrm{R}} + (R\vartheta\, c_{\mathrm{R}}^{\max})\left[\bar{c}\ln\bar{c} + (1-\bar{c})\ln(1-\bar{c})\right]. \tag{2.109}$$

Then

$$\frac{\partial\psi_{\mathrm{R}}}{\partial c_{\mathrm{R}}} = \Omega\left[\tfrac{1}{2}\mathbf{E}^e : \mathbb{C}\mathbf{E}^e\right] + \frac{\partial}{\partial c_{\mathrm{R}}}\left(J^{-1}\left(\frac{1}{2\varepsilon}\mathbf{d}_{\mathrm{R}}\cdot\mathbf{C}\mathbf{d}_{\mathrm{R}}\right)\right) + \mu_0 + R\vartheta\,\ln\left(\frac{\bar{c}}{1-\bar{c}}\right).$$

Since,

$$\begin{aligned}\frac{\partial}{\partial c_{\mathrm{R}}}\left(J^{-1}\left(\frac{1}{2\varepsilon}\mathbf{d}_{\mathrm{R}}\cdot\mathbf{C}\mathbf{d}_{\mathrm{R}}\right)\right) &= \frac{\partial}{\partial c_{\mathrm{R}}}\left(J^{e-1}J^{s-1}\lambda^{s2}\left(\frac{1}{2\varepsilon}\mathbf{d}_{\mathrm{R}}\cdot\mathbf{C}^e\mathbf{d}_{\mathrm{R}}\right)\right)\\ &= \frac{\partial}{\partial c_{\mathrm{R}}}\left(J^{e-1}J^{s-1/3}\left(\frac{1}{2\varepsilon}\mathbf{d}_{\mathrm{R}}\cdot\mathbf{C}^e\mathbf{d}_{\mathrm{R}}\right)\right)\\ &= -\frac{1}{6\varepsilon}J^{e-1}J^{s-4/3}\Omega\left(\mathbf{d}_{\mathrm{R}}\cdot\mathbf{C}^e\mathbf{d}_{\mathrm{R}}\right),\end{aligned}$$

and since

$$\mathbf{d}_{\mathrm{R}} = \varepsilon J\mathbf{F}^{-1}\mathbf{e} = \varepsilon J^e J^s\lambda^{s-1}\mathbf{F}^{e\,-1}\mathbf{e} = \varepsilon J^e J^{s2/3}\mathbf{F}^{e\,-1}\mathbf{e},$$

we have

$$\begin{aligned}\frac{\partial}{\partial c_{\mathrm{R}}}\left(J^{-1}\left(\frac{1}{2\varepsilon}\mathbf{d}_{\mathrm{R}}\cdot\mathbf{C}\mathbf{d}_{\mathrm{R}}\right)\right) &= -\frac{1}{6\varepsilon}J^{e-1}J^{s-4/3}\Omega\left(\varepsilon J^e J^{s2/3}\right)^2\left(\mathbf{F}^{e\,-1}\mathbf{e}\cdot\mathbf{C}^e\mathbf{F}^{e\,-1}\mathbf{e}\right),\\ &= -\frac{1}{6}\varepsilon J^e\Omega\left(\mathbf{e}\cdot\mathbf{e}\right),\end{aligned}$$

and hence,

$$\frac{\partial\psi_{\mathrm{R}}}{\partial c_{\mathrm{R}}} = \mu_0 + R\vartheta\,\ln\left(\frac{\bar{c}}{1-\bar{c}}\right) + \Omega\left[\tfrac{1}{2}\mathbf{E}^e : \mathbb{C}\mathbf{E}^e\right] - \frac{1}{6}\varepsilon J^e\Omega\left(\mathbf{e}\cdot\mathbf{e}\right).$$

Therefore, the electrochemical potential is given by

$$\omega = \mu_0 + R\vartheta\,\ln\left(\frac{\bar{c}}{1-\bar{c}}\right) + \Omega\, p + F\phi + \Omega\left[\tfrac{1}{2}\mathbf{E}^e : \mathbb{C}\mathbf{E}^e\right] - \frac{1}{6}\varepsilon J^e\Omega\left(\mathbf{e}\cdot\mathbf{e}\right)$$

Next,

$$\begin{aligned}p &= J^e\left(-\frac{1}{3}\operatorname{tr}\mathbf{T}\right)\\ &= -\frac{1}{3}K\left(\operatorname{tr}\mathbf{E}_{\mathrm{H}} - \ln J^s\right) + \frac{1}{6}\varepsilon\, J^e\,\mathbf{e}\cdot\mathbf{e}\\ &= -\frac{1}{3}K\left(\operatorname{tr}\mathbf{E}^e_{\mathrm{H}}\right) + \frac{1}{6}\varepsilon\, J^e\,\mathbf{e}\cdot\mathbf{e}\end{aligned}$$

and hence

$$\omega = \mu_0 + R\vartheta\,\ln\left(\frac{\bar{c}}{1-\bar{c}}\right) + \Omega\left(-\frac{1}{3}K\operatorname{tr}\mathbf{E}^e_{\mathrm{H}}\right) + F\phi + \Omega\left[\tfrac{1}{2}\mathbf{E}^e : \mathbb{C}\mathbf{E}^e\right].$$

Further, using $(2.60)_2$, (2.63), (2.87), the electrochemical potential ω is given by

$$\omega = \mu_0 + R\vartheta\,\ln\left(\frac{\bar{c}}{1-\bar{c}}\right) + \Omega\left(-\frac{1}{3}K\operatorname{tr}\mathbf{E}^e_{\mathrm{H}}\right) + F\phi + \Omega\left[\tfrac{1}{2}\mathbf{E}^e : \mathbb{C}\mathbf{E}^e\right]. \tag{2.110}$$

Henceforth, we set the reference chemical potential μ_0 to zero and we neglect the effects of the last term in (2.110), which is of quadratic order in the elastic strain $\mathbf{E}^e$ and anticipated to be smaller in magnitude than the other terms, in which case (2.110) reduces to

$$\boxed{\omega = R\vartheta \, \ln\left(\frac{\bar{c}}{1-\bar{c}}\right) + \Omega \left(-\frac{1}{3} K \operatorname{tr} \mathbf{E}^e_{\mathrm{H}}\right) + F\,\phi\,.} \tag{2.111}$$

2.12.6 Species flux

We assume that the *spatial flux* $\mathbf{j}$ of the hydrated cations depends only on the *spatial gradient* of its electrochemical potential and given by,

$$\mathbf{j} = -\mathbf{M}_s(c)\,\mathrm{grad}\,\omega, \tag{2.112}$$

with a spherical *spatial* mobility tensor

$$\mathbf{M}_s(c) = m(c)\mathbf{1}, \tag{2.113}$$

where

$$m(c) = \frac{Dc(1-\bar{c})}{R\vartheta} \geq 0 \tag{2.114}$$

is a positive-valued scalar mobility at a given temperature ϑ, with $D > 0$ representing a cation diffusion coefficient with units of $[\mathrm{m}^2/\mathrm{s}]$, and

$$c = J^{-1} c_{\mathrm{R}} \tag{2.115}$$

is the species concentration per unit volume of the deformed body.

2.12.7 Generalized Nernst-Planck equation

Next, from (2.111),

$$\mathrm{grad}\,\omega = \frac{R\vartheta}{c(1-\bar{c})}\,\mathrm{grad}\,c + \Omega\,\mathrm{grad}\,p + F\mathrm{grad}\,\phi, \tag{2.116}$$

and hence using (2.112), (2.114), and (2.116) the flux of the mobile species in the deformed body is given by

$$\boxed{\mathbf{j} = -D\left[\mathrm{grad}\,c + \left(\frac{Fc(1-\bar{c})}{R\vartheta}\right)\,\mathrm{grad}\,\phi + \left(\frac{\Omega c(1-\bar{c})}{R\vartheta}\right)\,\mathrm{grad}\,p\right].} \tag{2.117}$$

This equation has the same form as the **Nernst-Planck** equation commonly used to describe the migration of a chemical species in a fluid under an electric field. It describes the flux of ions as the sum of the diffusive component which is related to the gradient of the concentration, $\mathrm{grad}\,c$, and a migrative component associated with the gradient of the electric potential $\mathrm{grad}\,\phi$, and another migrative component associated with the gradient of the mechanical pressure $\mathrm{grad}\,p$.

2.13 Governing partial differential equations expressed spatially

1. **Equation of equilibrium**:

   The equation of equilibrium in the absence of body forces is,

   $$\operatorname{div}\mathbf{T} = \mathbf{0}, \tag{2.118}$$

   where the Cauchy stress $\mathbf{T}$ is given by (2.107).

2. **Gauss's law**:

   This is given by

   $$\operatorname{div}\mathbf{d} = q \qquad \text{with} \qquad q = F\,(c - c_0), \tag{2.119}$$

   with $\mathbf{d}$ given by (2.90). Equation (2.119) for a homogeneous material may be written as

   $$\Delta\phi = -\frac{F}{\varepsilon}\,(c - c_0)\,, \tag{2.120}$$

   with the effective electrical permittivity ε given by

   $$\varepsilon = \varepsilon_r\,\varepsilon_0\,, \tag{2.121}$$

   where ε_r is a *relative electrical permittivity*, and $\varepsilon_0 = 8.85 \times 10^{-12}\,\mathrm{F/m}$ is the electrical permittivity of vacuum.

3. **Mass balance**:

   Mass balance for the migrating cationic species is given by

   $$\dot{c}_{\mathrm{R}} = -J\operatorname{div}\mathbf{j}, \tag{2.122}$$

   with $\mathbf{j}$ given by (2.112), viz.

   $$\mathbf{j} = -\left(\frac{Dc(1-\bar{c})}{R\vartheta}\right)\operatorname{grad}\omega, \tag{2.123}$$

   with the electrochemical potential ω given by (2.111).

2.14 Boundary and initial conditions

Next, we consider the boundary conditions.

1. **Boundary conditions for the partial differential equation (pde) governing the mechanical displacement**:

   With the spatial description of displacement given by $\mathbf{u}(\mathbf{x},t) = \mathbf{x} - \boldsymbol{\chi}^{-1}(\mathbf{x},t)$, let $\mathcal{S}_{\mathbf{u}}$ and $\mathcal{S}_{\mathbf{t}}$ be complementary subsurfaces of the boundary $\partial\mathcal{B}_t$ of the body $\mathcal{B}_t$. Then for a time interval $t \in [0,T]$ we consider a pair of boundary conditions:

   $$\begin{aligned} \mathbf{u} &= \breve{\mathbf{u}} \quad \text{on } \mathcal{S}_{\mathbf{u}} \times [0,T], \\ \mathbf{T}\mathbf{n} &= \breve{\mathbf{t}} \quad \text{on } \mathcal{S}_{\mathbf{t}} \times [0,T]. \end{aligned} \tag{2.124}$$

   In the boundary conditions above $\breve{\mathbf{u}}$ and $\breve{\mathbf{t}}$ are *prescribed* functions of $\mathbf{x}$ and t.

2. **Boundary conditions for the pde governing the electric potential**:

   Let $\mathcal{S}_\phi$ and $\mathcal{S}_\varpi$ be complementary subsurfaces of the boundary $\partial\mathcal{B}_t$ of the body $\mathcal{B}_t$. Then for a time interval $t \in [0,T]$ we consider a pair of boundary conditions:

   $$\begin{aligned} \phi &= \breve{\phi} \quad \text{on } \mathcal{S}_\phi \times [0,T], \\ -\mathbf{d}\cdot\mathbf{n} &= \breve{\varpi} \quad \text{on } \mathcal{S}_\varpi \times [0,T]. \end{aligned} \tag{2.125}$$

   In the boundary conditions above $\breve{\phi}$ and $\breve{\varpi}$ are the *prescribed* electric potential and surface charge density.

3. **Boundary conditions for the pde governing the mass balance**:

   With $\mathcal{S}_\omega$ and $\mathcal{S}_{\mathbf{j}}$ complementary subsurfaces of the boundary $\partial\mathcal{B}_t$ of the body $\mathcal{B}_t$ we consider a pair of boundary conditions:

$$\begin{aligned} \omega &= \breve{\omega} \quad \text{on } \mathcal{S}_\omega \times [0,T], \\ -\mathbf{j}\cdot\mathbf{n} &= \breve{j} \quad \text{on } \mathcal{S}_{\mathbf{j}} \times [0,T], \end{aligned} \tag{2.126}$$

   with $\breve{\omega}$ and $\breve{j}$ prescribed electrochemical potential and cation flux.

The initial data is taken as

$$\mathbf{u}(\mathbf{X},0) = \mathbf{0}, \qquad \text{and} \qquad \phi(\mathbf{X},0) = \phi_0,$$

and we require that initially *charge neutrality* hold, so that

$$c_{\mathrm{R}}(\mathbf{X},0) = c_{\mathrm{R}0}(\mathbf{X},0) \equiv \underbrace{c_{\mathrm{R}0}}_{\text{fixed}}, \tag{2.127}$$

which will impose appropriate initial conditions on the corresponding electrochemical potential,

$$\omega(\mathbf{X},0) = \omega_0(\mathbf{X}).$$

2.15 Numerical implementation

We have numerically implemented our theory as a user-element (UEL) subroutine in the implicit finite element program Abaqus/Standard (Abaqus, 2017) by following the implementation procedures detailed in Chester et al. (2015). We have developed our UEL for four-noded axisymmetric and plane-strain quadrilateral elements as well as eight-noded full 3-D hexahedral elements.

3 Application of the theory to Nafion-based IPMCs

In this section we apply our theory to model the response of Nafion-based IPMCs:

- We first calibrate the material parameters in the theory by using results from certain experiments using step-voltage inputs reported by Nguyen et al. (2007).
- We then show the predictive capabilities of the calibrated model for a sinusoidal voltage inputs by comparing the results from simulations against corresponding experiments also reported in Nguyen et al. (2007) on the same IPMC.

3.1 Material parameters

We have estimated the material parameters in our theory for a Nafion-based IPMC by attempting to simulate the results from the following experiments using step-voltage inputs reported by Nguyen et al. (2007):

- Curling of a cantilevered beam (cf. Section 3.2), and
- Blocking force response of a constrained beam (cf. Section 3.3).

The calibrated list of material parameters is summarized in Table 1.[10]

Table 1: Material parameters for a Nafion-based IPMC at room temperature $\vartheta = 298$K.

Material parameter	**Value**	**Units**
E	78	MPa
ν	0.3	-
Ω	1.04×10^{-4}	$\mathrm{m}^3/\mathrm{mol}$
D	1.3×10^{-11}	m^2/s
c_0	1,500	$\mathrm{mol}/\mathrm{m}^3$
$c_{\mathrm{R}}^{\max}$	10,000	$\mathrm{mol}/\mathrm{m}^3$
ε_r	120	-

Remarks: Our rationales for this choice for the values of the material parameters is briefly discussed below.

- Values of the Young's modulus E,[11] the molar volume Ω, and the diffusivity D for the membrane are all calibrated to fit the experiments described in Sections 3.2 and 3.3.
- The Young's modulus for a hydrated Nafion membrane is reported in the literature (cf., e.g., Nemat-Nasser, 2002; Kim and Shahinpoor, 2003; Satterfield and Benziger, 2009) to be in the range of 50-200 MPa. Our calibrated value of 78 MPa lies well in this range. For the Poisson's ratio, we have chosen a standard value of 0.3.

  Also, since there is not much information available regarding the mechanical properties of platinum-infused electrode regions, for simplicity we take the stiffness of the electrodes to be *identical* to that of the bulk electrolyte.[12]
- Our calibrated value of molar volume for the *hydrated lithium ions* in the Nafion membrane is $\Omega = 1.04 \times 10^{-4}$ $\mathrm{m}^3/\mathrm{mol}$. This value is higher in comparison to the molar volumes of lithium metal and water which are 1.3×10^{-5} and 1.8×10^{-5} $\mathrm{m}^3/\mathrm{mol}$, respectively.
- The calibrated value of the diffusivity parameter D is $\sim 10^{-11}$ m^2/s, which is in the range of expected values for room temperature diffusivities.
- The proton capacity of the synthesized Nafion membrane reported in Nguyen et al. (2007) is 0.95 mmol/g. Given the density of Nafion is about 1.58 g/cm^3 (Zook and Leddy, 1996), the initial cation concentration can be estimated as $c_0 \approx 1,500$ $\mathrm{m}^3/\mathrm{mol}$.
- We use $c_{\mathrm{R}}^{\max} = 10,000$ $\mathrm{mol}/\mathrm{m}^3$ for the saturation value of the concentration of cations. Similar concentration saturation values have been used in the literature for other Li^+ systems (cf., e.g., Salvadori et al., 2015).

[10] We have used these material parameters in all the simulations of Nafion-based IPMCs reported in this paper.

[11] $E = 9KG/(3K + G)$, and $\nu = (3K - 2G)/2(3K + G)$.

[12] The micrographs reported by Nemat-Nasser (2002) show that the volume fraction of platinum particles in the infused electrode regions is quite small. These sparsely distributed platinum particles are not expected to contribute to a large change in the stiffness of the electrode regions relative to that of the bulk of the Nafion membranes.

- The relative permittivity of Nafion was reported as $\varepsilon_r \approx 120$ in Wallmersperger et al. (2008a) using electrical measurements on a Nafion-dielectric based capacitor.

  Dimensional analysis of the Poisson equation (2.120), viz.

$$\Delta\phi = -\frac{F}{\varepsilon_r \varepsilon_0}\,(c - c_0)\,, \tag{3.1}$$

  leads us to certain conclusions. Normalising the potential ϕ by the "thermal volt" $R\vartheta/F$ and the spatial concentration of cations c by the initial concentration c_0,

$$\phi^* \stackrel{\text{def}}{=} \frac{\phi}{(R\vartheta/F)}, \qquad c^* \stackrel{\text{def}}{=} \frac{c}{c_0}, \tag{3.2}$$

  we may rewrite (3.1) as

$$2\,\lambda^2_{\text{Debye}}\Delta\phi^* + (c^* - 1) = 0, \tag{3.3}$$

  where the length scale

$$\lambda_{\text{Debye}} \stackrel{\text{def}}{=} \sqrt{\frac{\varepsilon_r \varepsilon_0 R\vartheta}{2F^2 c_0}} \tag{3.4}$$

  is commonly called the *Debye length*. In numerical simulations we have to contend with trying to resolve two boundary layers, one close to the top surface of the membrane and one near the bottom surface, where the cation concentration is significantly different from the fixed anion concentration. These regions over which deviation from electroneutrality occurs are of the order of a few Debye lengths in thickness. Unfortunately these boundary layers are only $\sim 1.5\,\text{nm}$ thick, and the resolution of such thicknesses in a 300 micron thick membrane is computationally not tractable. To overcome this numerical difficulty, in our simulations we have modified (2.120) by introducing a *numerical permitivity factor* ε_{num},

$$\Delta\phi = -\frac{F}{\varepsilon_{\text{num}}\varepsilon_r \varepsilon_0}\,(c - c_0)\,, \tag{3.5}$$

  so that

$$\lambda_{\text{Debye,num}} \stackrel{\text{def}}{=} \sqrt{\frac{\varepsilon_{\text{num}}\varepsilon_r \varepsilon_0 R\vartheta}{2F^2 c_0}} \tag{3.6}$$

  represents a *numerically enhanced* Debye length. We have used a value of $\varepsilon_{\text{num}} = 10^7$ in our simulations, and in this case the thickness of boundary layers is increased to $\sim 5\mu\text{m}$ which represents about $\sim 1.5\%$ of the total membrane thickness — and therefore resolvable with a computationally tractable number of finite elements. An additional discussion of the use of the ε_{num} factor is given in Appendix A.

  We emphasize that:

  - We have used the ε_{num} factor only in the Poisson equation (3.5).
  - We **do not** use this factor in equation (2.107) for the Cauchy stress, which would artificially enhance the effects of the Maxwell stress.

3.2 Curling response of a cantilevered Nafion IPMC beam subjected to a step-voltage

Nguyen et al. (2007) have reported on several experiments on Nafion-based IPMCs with mobile Li^+ cations, and platinum-infused electrodes. Fig. 2 shows a schematic of their cantilevered beam specimens subjected to a "step" voltage input. The beams in their experiments had a total length of 20 mm, a width of 5 mm, and a thickness of 300 μm. The electrodes were reported to be 7-8 μm thick, so in our simulations we have used an electrode thickness of 7.5 μm. In our simulations we model the beam under plane-strain conditions, and do not permit any flux of cations at the boundaries of the membrane. The lower electrode is grounded, i.e. set to a reference voltage of 0 V. As shown in Fig. 2(b), a step voltage input of 3 V is applied on the upper surface and held fixed for a time period of 20 s.[13]

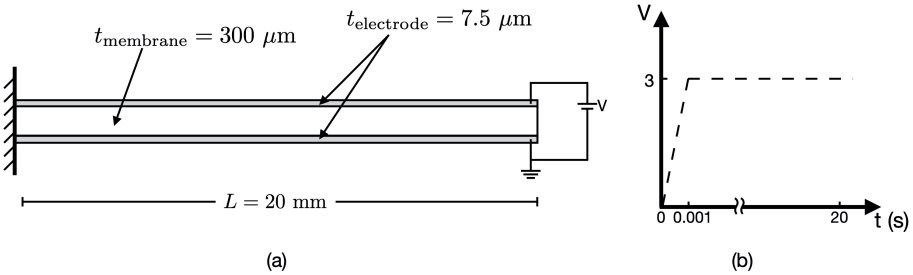

Figure 2: Curling of a cantilevered beam: (a) schematic of the initial geometry; (b) voltage input.

The finite element mesh employed in our calculations is shown in Fig. 3. The mesh for the membrane consists of 300 uniformly spaced elements across its length, and 120 elements across its thickness with a biased spacing. The density of elements is higher towards the top and bottom surfaces of the membrane, with successive element sizes of ratio 1.07. The higher mesh density at the two ends of the membrane is used to resolve the large gradients in electrostatic potential and cation concentration at the boundaries, as we discuss in the rest of this section. The meshes for the two electrodes each consist of 4 uniformly spaced elements across their thickness, and 300 uniformly spaced elements along their length.

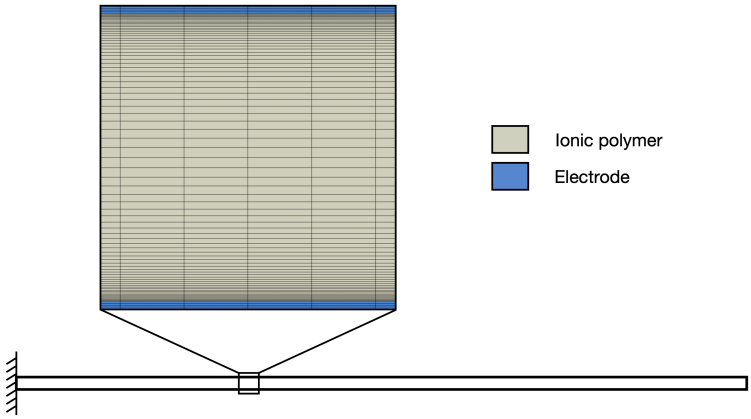

Figure 3: Scale drawing of the IPMC actuator under study with detailed view of the mesh.

[13] In our simulations we use a 1 ms "smooth step" amplitude profile to apply the step in electric potential. This amplitude profile is a modified ramp function whose first and second time derivatives are zero at $t = 0$ and $t = 1$ ms.

Figs. 4(a) and (b) respectively show the variation of the electrostatic potential ϕ and the normalized cation concentration $\bar{c}$ across the thickness of the membrane at time $t = 1\,\text{ms}$ when the voltage has just been ramped up to 3 V. In these plots, the field of interest is plotted on the horizontal axis and the membrane thickness is plotted on the vertical axis, such that the lower end of the plot at $y = 0$ represents the bottom surface of the membrane while the upper end of the plot at $y = 300\,\mu\text{m}$ represents the top surface of the membrane. At this instant, Fig. 4(a) shows that the variation of ϕ is nearly linear and thus the electric field is a constant pointing from the top surface to the bottom. Fig. 4(b) shows that normalized concentration through the membrane thickness is still unchanged from its initial value of $\bar{c} = 0.15$.

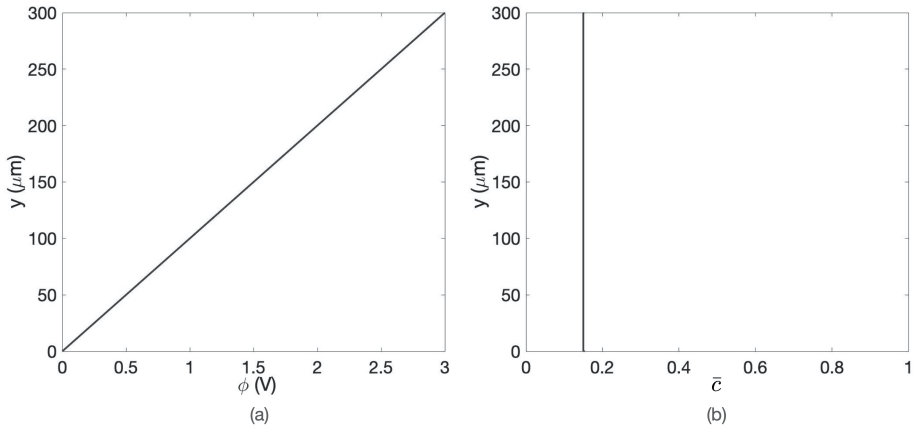

Figure 4: Profiles of: (a) electrostatic potential ϕ, and (b) normalized concentration $\bar{c}$ across the thickness of the membrane at $t = 1\,\text{ms}$ when the voltage has just been ramped up to 3 V.

The gradient in the electric potential drives the migration of the cations from the top of the membrane to the bottom of the membrane. The resulting concentration profile in the membrane evolves over time. The variation in the normalized concentration $\bar{c}$ across the thickness of the membrane is shown in Fig. 5(a)-(f) at different instants of time. Fig. 5(a) shows that at 10 ms, there is a small increase in the concentration $\bar{c}$ near the bottom, and a decrease near the top. As time evolves, larger deviations of $\bar{c}$ from its initial value of 0.15 can be observed as shown in Fig. 5(b) through (f). The value of $\bar{c}$ cannot exceed a value of 1, nor can it be lower than 0. When these limiting values are reached at the boundaries, further migration of ions results in depleted regions at the top with $\bar{c} = 0$ — see Fig. 5(d)-(f), and saturated regions at the bottom with $\bar{c} = 1$ — see Fig. 5(e)-(f). The large gradients in the concentration of cations exist over a few (three to five) Debye lengths, $\lesssim 5\ \mu$m, at all instants. Over the bulk of the electrolyte, the concentration of cations remains close to the initial values, which is the same concentration as the fixed anions. The redistribution of cations ceases after $\sim 12\,\text{s}$, and the membrane reaches a steady state shown in Fig. 5(f) at a time of 20 s.

The simultaneous evolution of the electrostatic potential ϕ in the membrane is shown in Fig. 6. Initially, the electrostatic potential distribution is nearly linear, with a small non-linearity starting to appear at 750 ms at the boundaries; cf. Fig 6(c). After 1.5 s, cf. Fig. 6(d), the non-linear variation in ϕ at the boundaries becomes evident. There are larger gradients in the potential in the boundary regions than in the bulk, especially at the upper boundary where a substantial depleted region has developed at this instant (see Fig. 5(d)). With increasing time the electric potential gradient at the boundaries becomes increasingly larger than the gradient in the bulk, and the width of this region also increases. At steady state, shown in Fig. 6(f), the electric potential is nearly constant in the bulk of the membrane, while all the changes in potential occur in the regions where the concentrations deviated from the initial value in Fig. 5(f).

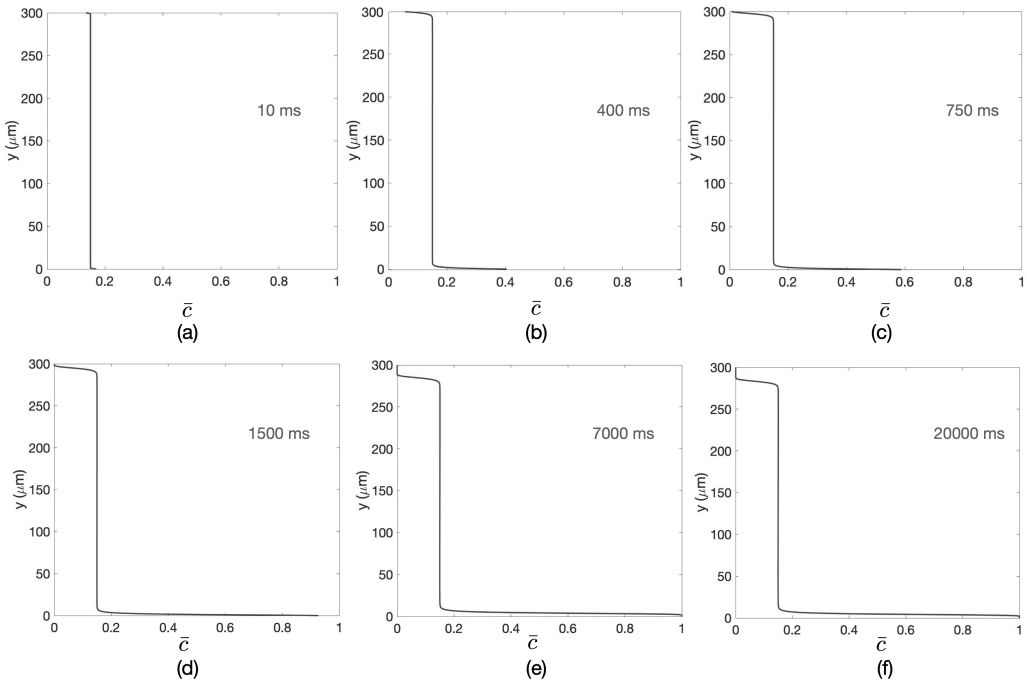

Figure 5: Variation of the normalized concentration $\bar{c}$ through the thickness of the membrane at: (a) 10 ms, (b) 400 ms, (c) 750 ms, (d) 1.5 s, (e) 7 s, (e) 20 s.

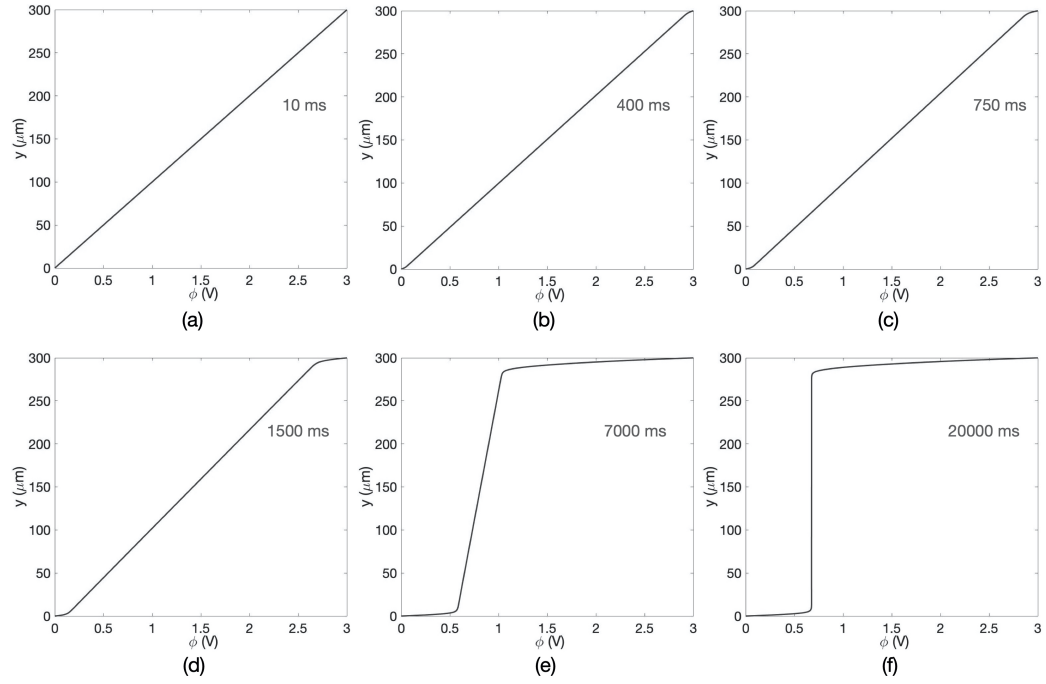

Figure 6: Electrostatic potential variation through the thickness of the beam at (a) 10 ms (b) 400 ms (c) 750 ms (d) 1.5 s (e) 7 s (e) 20 s.

The grey-blue lines in Figs. 7(a) and (b), taken from Nguyen et al. (2007), show the experimentally observed initial and curled shapes of a cantilevered Nafion IPMC membrane at times $t = 0\,\text{s}$ and $t = 20\,\text{s}$. The overlayed bright green lines in these figures show the corresponding results from our simulations. As described earlier, the concentration of the hydrated cations in the membrane evolves with time in response to the applied step voltage. As the concentration of the cations increases near the bottom of the membrane it is accompanied by chemical expansion; cf. eq.(2.96). Similarly the upper part of the membrane experiences compressive strains since the cation concentration in this region decreases as time increases. This differential swelling leads to a bending deformation in the specimen towards the top electrode (the anode). The amount of curling of the cantilevered beam at 20 s depends strongly on the value of the molar volume Ω of the hydrated cations and also the stiffness of the membrane, with the former being the more dominant factor. We calibrated the value of Ω in our theory to fit the experimentally observed deformed geometry shown in Fig. 7(b). The excellent fit of the curled shape seen in Fig. 7 was obtained for a value of

$$\Omega = 1.04 \times 10^{-4}\ \text{m}^3/\text{mol},$$

together with of course the values of the other material parameters listed in Table 1.

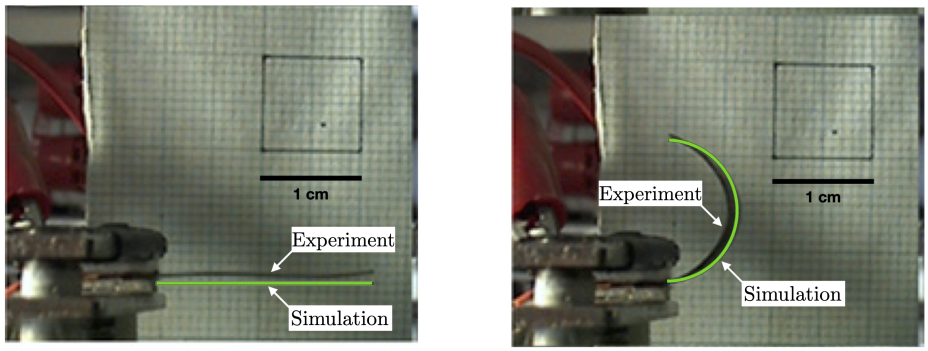

(a) t = 0 s (b) t = 20 s

Figure 7: This figure, adapted from Nguyen et al. (2007) shows the experimentally observed shapes of a cantilevered Nafion IPMC membrane at: (a) $t = 0\,\text{s}$ and (b) $t = 20\,\text{s}$. The overlayed bright green lines are the corresponding results from our simulations (color online).

- A movie of the time-dependent bending deformation of the beam from our simulations is shown in *Supplementary Video 1.*

Remark. Before closing this section we note that the effect of the Maxwell stress on curling of an IPMC beam is negligible in comparison to the effect of the chemo-mechanical stress. In order to verify this assertion, we have repeated the simulation of the curling of a cantilevered beam by: (i) including the Maxwell stress term, as discussed above, and by (ii) completely suppressing the Maxwell stress term by setting the electrostatic stress in eq. (2.106) to zero, $\mathbf{T}^{(\text{es})} = \mathbf{0}$. Fig. 8 shows the history of the x- and y-direction displacements of the tip (the middle node of the free edge) of the beam from these two simulations.[14] The results from the two simulations are *nearly identical*, which demonstrates that the Maxwell stress with the actual value of the permittivity $\varepsilon = \varepsilon_r \varepsilon_0$ does not have a significant influence on the response of the beam.

[14]The peak in the y-displacement of the tip is due to the large curling of the IPMC — as the curled actuated shape evolves beyond a semi-circle, the y-displacement changes direction even though the overall actuation has not changed direction.

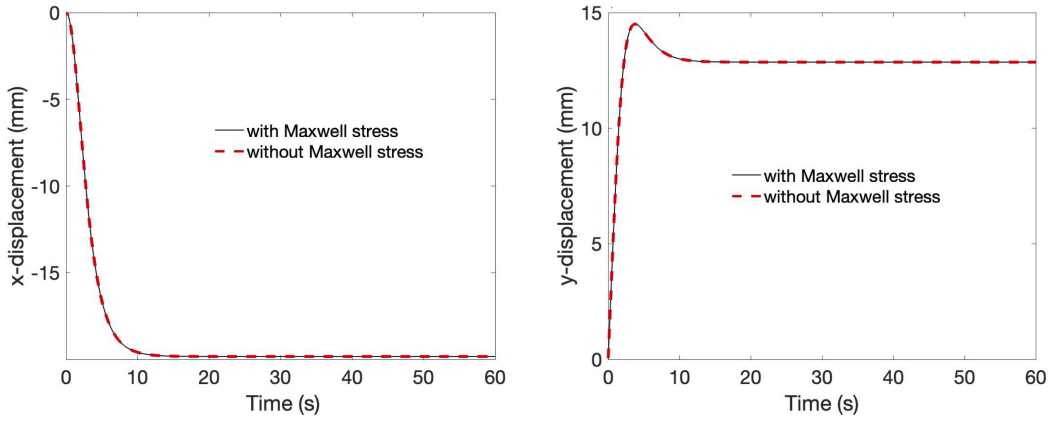

Figure 8: Displacement history of the tip (middle node of right edge) in both the x- and y-directions for simulations with and without inclusion of the Maxwell stress.

3.3 Blocking force response of a constrained Nafion IPMC beam subjected to a step-voltage

Nguyen et al. (2007), using a Nafion IPMC specimen similar to that discussed in the previous subsection, also measured the blocking force generated by the beam under the same step-actuation voltage, but using a constrained geometry shown schematically in Fig. 9(a). The right edge of the specimen is free to rotate and also to translate in the horizontal direction, but it is constrained not to move in the vertical direction. We have numerically simulated such an experiment. As in the previous simulation, the voltage is ramped up to a value of 3 V over a period of 1 ms and held constant thereafter; cf. Fig. 2(b). The evolution of the profiles of the cation concentration $\bar{c}$ and electric potential ϕ are similar to those described in the previous subsection. However, here, since the right end of the beam is constrained, the beam cannot undergo free bending as in the previous case. The deformed geometry of the constrained beam specimen from our simulation at steady state is shown in Fig. 9(b).

- A movie of the simultaneous evolution of the blocking force and the deformation of the specimen from our simulations is shown in *Supplementary Video 2*.

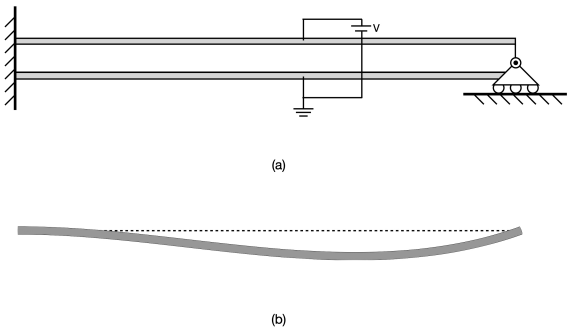

Figure 9: (a) A schematic of the geometry and boundary conditions for the constrained beam for the blocking force simulation. (b) Numerically predicted deformed shape of the IPMC beam at steady state. The horizontal dashed line indicates the axis of the actuator in the undeformed configuration.

The force exerted by the beam on the support maintaining the constraint in the vertical direction was measured and reported in Nguyen et al. (2007); it is shown in Fig. 10 as the black circles. The solid line in this figure is the corresponding result from our simulation. Starting from zero, the blocking force increases during the time over which the cation redistribution occurs. In our simulations the blocking force increases and then saturates at a constant value once steady state is reached. However in their experiments, Nguyen et al. observed some relaxation which they attributed to loss of solvent molecules from the hydrated membrane to the surrounding environment. In our model we have not accounted for this second-order loss of water molecules to the surroundings, and hence we concentrate here only on the steady state response for our material parameter calibration efforts.

Two important features of the blocking force evolution shown in Fig. 10 are: (i) the peak force, and (ii) the amount of time taken to reach this value. Our simulations show that the value of the peak force is strongly dependent on the value of the stiffness E of the membrane, as well as the molar volume Ω of the hydrated cations. Since we have already calibrated a value for Ω in the previous subsection, we used the magnitude of the peak force to calibrate the stiffness E of the membrane. Also, we used the time to reach given peak force to calibrate a value of the diffusivity D of the the hydrated cations. As seen from the comparison plot in Fig. 10, the calibrated values of

$$E = 78\,\text{MPa} \quad \text{and} \quad D = 1.3 \times 10^{-11}\ \text{m}^2/\text{s},$$

fit the experimental response quite well.

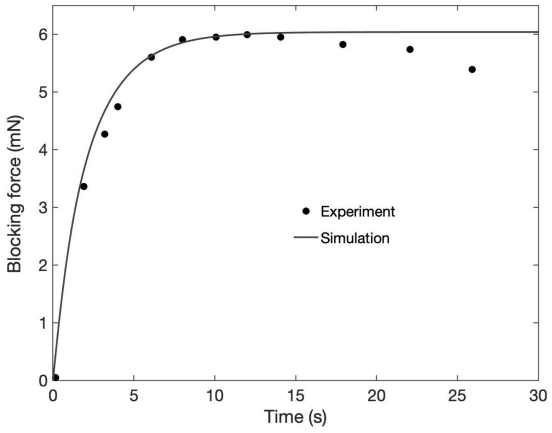

Figure 10: Blocking force response from our simulations shown as the solid line and the experiments of Nguyen et al. (2007) shown as black filled circles.

3.4 Predictive capability of the calibrated model

With the material parameters of the theory calibrated in the previous two sections, in this section we check the predictive capability of the theory for modeling the response of a cantilever IPMC beam to a sinusoidal voltage input. Specifically, we simulate the response of an unconstrained cantilevered beam — as in Fig. 4(a) — in which we prescribe a 1 Hz sinusoidal actuation voltage of an amplitude of 3 V, and compare the predicted response against the corresponding experimental response reported in Nguyen et al. (2007).

The numerically-predicted tip displacement is shown in Fig. 11 for the first 60 cycles. The displacement in the positive and negative directions over the first few cycles is evidently not symmetric about the zero tip displacement state. This is because the initial polarity of the applied voltage biases the deformation. With an increasing number of cycles the asymmetry gradually decreases as the influence of the initial state decays out. After about 50 cycles, the tip displacements have reached a steady-state response, which is shown in Fig. 12. At steady state the displacements are sinusoidal with the same frequency as the input voltage. Since there is a time delay associated with the migration of the cations following an applied voltage and the subsequent bending deformation (which is a result of the cation redistribution), Fig. 12 shows that there is a consistent phase lag between the output displacements and the input voltage.

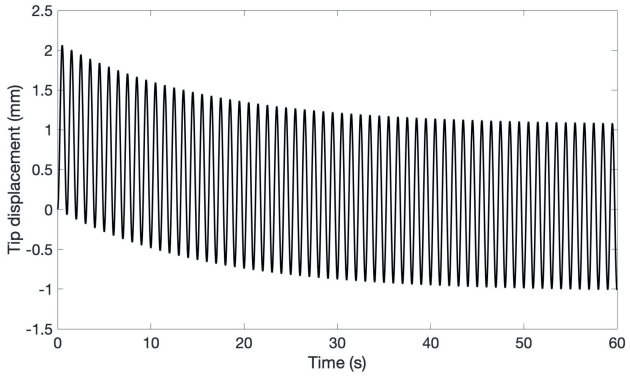

Figure 11: Tip displacement response over 60 cycles for a cantilevered beam subjected to a 0 to 3 V, 1 Hz sinusoidal voltage input.

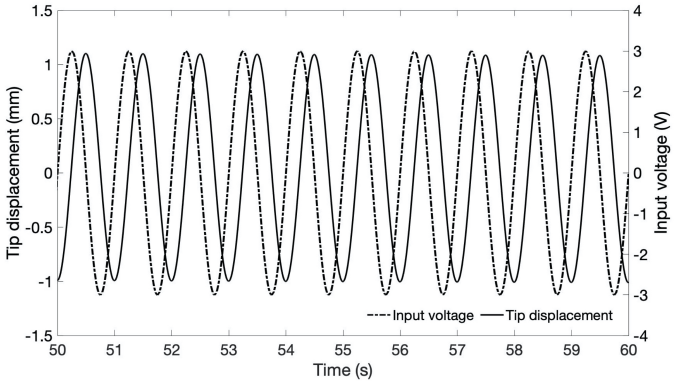

Figure 12: Tip displacement response from 50-60 cycles for a cantilevered beam subjected to a 0 to 3 V, 1 Hz sinusoidal voltage input.

- *Supplementary Video 3* shows the steady-state deformation of the cantilevered beam in response to the sinusoidal voltage input from our simulations.

In Fig. 13 we show a comparison of our prediction of the steady-state tip displacement against the corresponding experimental response reported in Nguyen et al. (2007). The agreement is excellent. The satisfactory prediction of the response in this experiment serves as a (partial) validation of the predictive capabilities of our theory and numerical simulation capability.

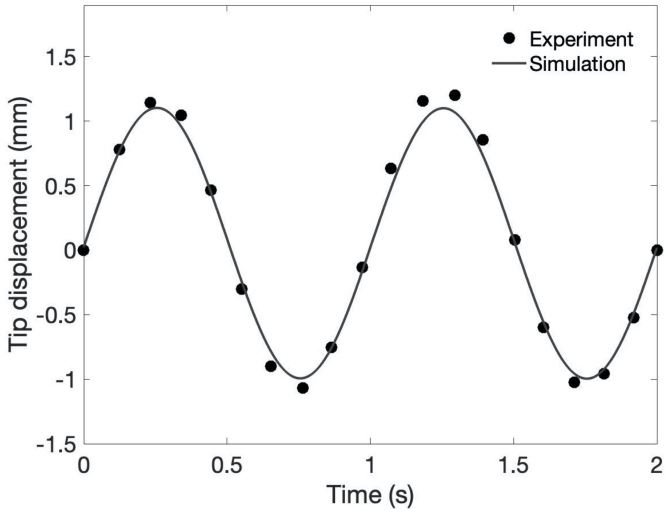

Figure 13: Comparison of predicted tip displacement at steady state against the experimentally-measured response (Nguyen et al., 2007).

4 Actuator Applications

To demonstrate the robustness of our numerical simulation capability, in this Section, using the eight-noded hexahedral finite-element implementation of our theory, we carry out full 3D simulations of two soft-robotics applications with some geometric complexity: (i) aquatic fins, and (ii) grippers.

4.1 Bio-inspired aquatic fin actuator

By embedding IPMC strip actuators into a soft "boot" material to create an active control surface — called a "fin", Palmre et al. (2013) have demonstrated the use of IPMCs in the design of bio-inspired fins. Depending on the orientation and placement of the actuators in the "boot", such fins can be used to realize complex deformations. In a particular realization of their bio-mimetic fin, they measured a maximum tip displacement of approximately 44 mm, and a twist angle which exceeded 10°. Fig. 14(a) shows a photograph of their experimental set-up of a fin, and Fig. 14(b) shows two views depicting twisting angle achieved in their experiments. Also, see `https://www.youtube.com/watch?v=qFV65SmFHLA` for a video of their fin actuator. Their results suggest that such active fin designs can be used for developing active propeller blades or control surfaces on underwater vehicles.

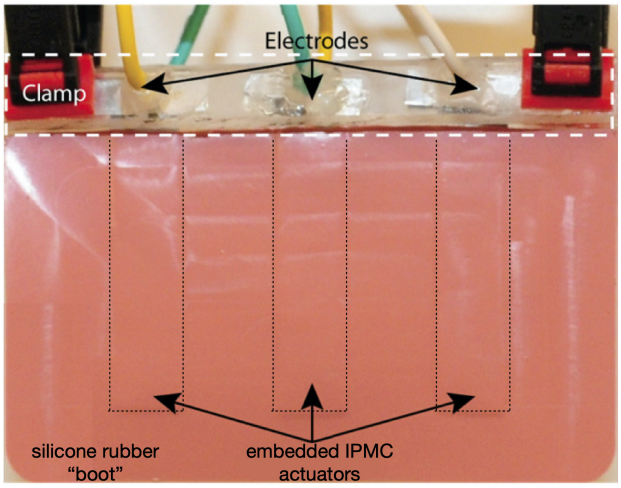

(a)

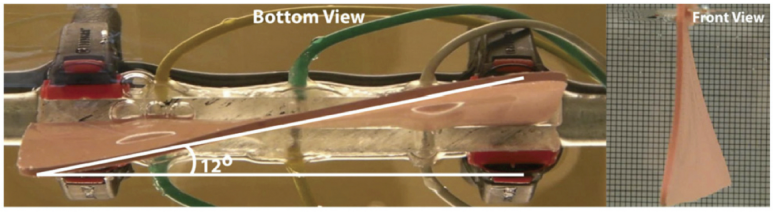

(b)

Figure 14: (a) Photograph of the experimental set-up of a fin made from a silicone boot with embedded IPMC actuators, from Palmre et al. (2013). (b) Two views depicting the twisting angle achieved by Palmre et al. in their experiments.

In this Section we report on our simulations of bending and twisting of a fin made from two Nafion IPMC actuators embedded in a silicone-based elastomeric matrix — the "boot".[15] A schematic of our simulation setup is shown in Fig. 15. The elastomeric boot has dimensions of 20 mm × 20 mm × 0.3 mm, and the two embedded IPMC actuators are each of dimensions 15 mm × 3 mm × 0.3 mm with an in plane separation of 8 mm. The two IPMC actuators can be individually controlled such that:

- When voltage inputs of positive polarity are applied on both IPMCs, then it results in upward bending of the fin.
- When voltage inputs of negative polarity are applied on both IPMCs, then it results in downward bending of the fin.
- When a positive voltage input is applied on one IPMC and a negative voltage to the other, it results in a twisting motion of the fin, since the individual IPMCs tend to move the fin in opposite directions.

Simulations of the deformed geometry of the fin under different applied positive and negative voltages of magnitude 1 V on each of the two IPMCs is shown in Fig. 16.

- A video of the simulations of the response of the fin to these different input voltages is provided as the file *Supplementary Video 4*.

[15]The silicone elastomer is modeled as an almost incompressible neo-Hookean material with a shear modulus of 1 MPa.

Accurate control of the geometry of the fin through the application of suitable input voltages makes such a system of use as a control surface for both underwater and aerial robotics applications.

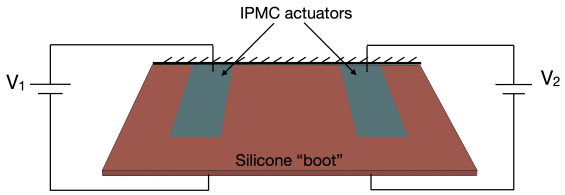

Figure 15: Schematic of a fin showing two Nafion-based IPMC actuators embedded in a silicone boot.

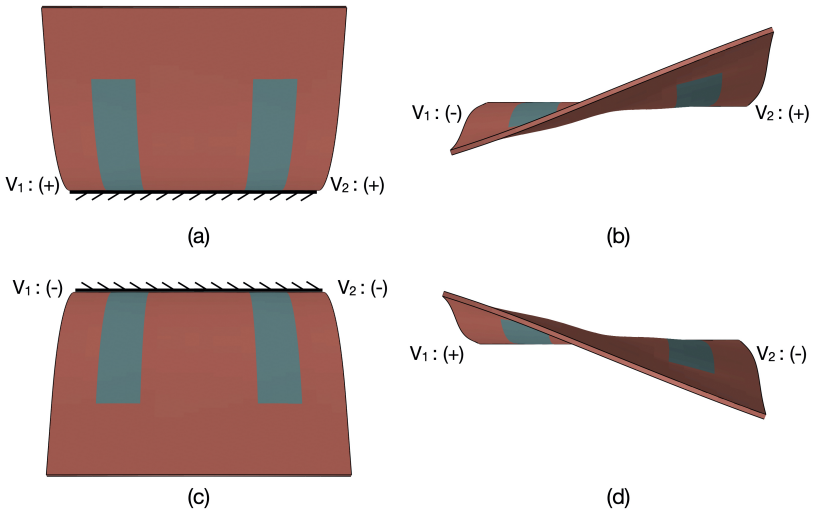

Figure 16: Deformed configurations of the fin for different applied voltages on the two actuators: (a) both input voltages positive; (b) negative voltage input on the left IPMC and positive input on the right IPMC; (c) both input voltages negative; and (d) positive input voltage on the left IPMC and negative input on the right IPMC.

4.2 A micro-gripper

In their classic 1998 review paper, Shahinpoor et al. (1998) showed an application of IPMCs which emulates a gripper with "fingers". Fig. 17(a) from their paper shows a gripper that uses IPMC fingers. The fingers are shown as vertical gray plates and the electrical wiring, where the films are connected back-to-back, can be seen in the middle portion of Fig. 17(a). This gripper was mounted on a 5 mm diameter graphite/epoxy composite rod to emulate a light-weight robotic arm. Upon electrical activation the fingers of the gripper can bend either inward or outward — similar to the operation of a hand — and thus close or open the gripper fingers as desired. Their four-finger gripper shown in Fig. 17(a) was able to lift a mass of 10.3 g. The demonstration of this gripper's capability to lift a rock was intended to pave the way for a potential future application of the gripper to planetary sample collection tasks — such as Mars exploration — where the low mass and low power consumption of an IPMC-based gripper offers distinct performance advantages.

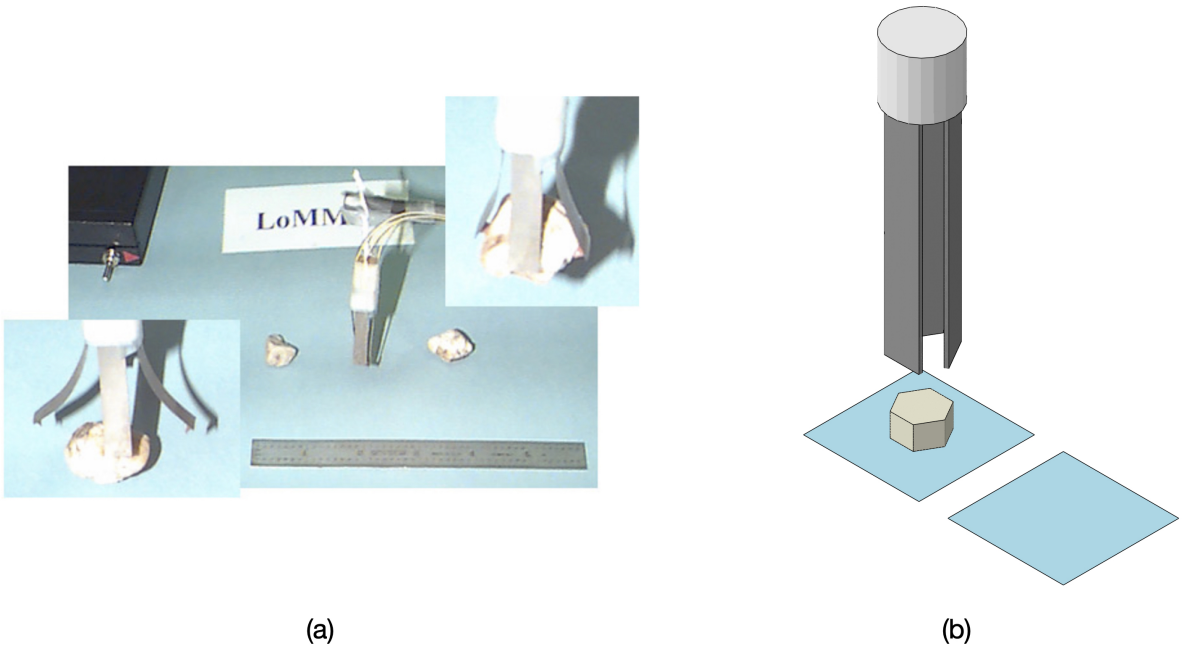

Figure 17: (a) An IPMC-based gripper from Shahinpoor et al. (1998). (b) The geometry of a three-finger IPMC-based gripper used in our simulation.

In this section we simulate the response a Nafion-based IPMC-based gripper similar to the one demonstrated by Shahinpoor et al. (1998), but with three-arms as shown in Fig. 17(b). The three IPMC actuators are each of dimensions $20 \times 3 \times 0.3$ mm. We simulate a pick-and-place operation of a hexagonal object of mass 0.05 g, from one platform to another. The hexagonal object is henceforth called the "specimen". The contact conditions between the IPMC fingers and the specimen are modeled as frictional contact with a Coulomb friction coefficient of 0.3.

- A video of the simulation of the pick-and-place operation is shown in *Supplementary Video 5*.

Fig. 18 shows snapshots of the gripper and specimen at various stages of the simulation. The initial position is shown in Fig. 18(a). As the gripper is moved toward the specimen, a positive voltage is applied on the outer surfaces of the IPMCs while keeping the inner surfaces grounded, which results in an outward curling of the individual IPMCs which opens the fingers of the gripper as it descends towards the specimen, Fig. 18(b). After the gripper is positioned to grab the specimen, the polarity of the applied voltage is reversed to close the fingers resulting in frictional contact with the specimen, as shown in Fig. 18(c). The frictional forces overcome the weight of the specimen as it is lifted and then manually moved by translating the gripper assembly towards the second platform, as shown in Fig. 18(d) and (e). Finally, the polarity of applied gripping voltage is reversed again which results in a curling of the fingers in the opposite direction so that the specimen is released, after which the gripper moves away, as shown in Fig. 18(f).

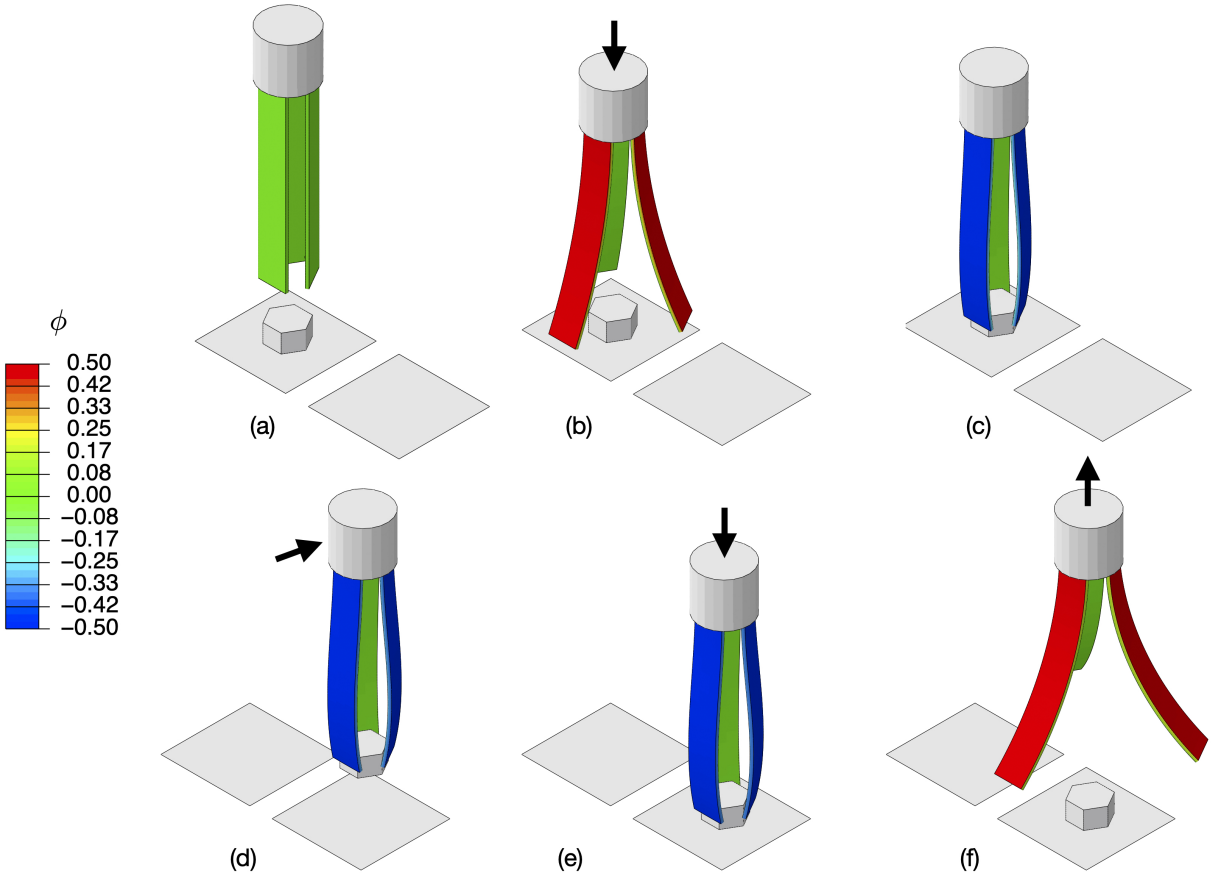

Figure 18: Snapshots of the IPMC-based gripper at various stages of the pick-and-place simulation. For ease of viewing of the contours of electric potential on the three IPMC "fingers", the electrodes have been excluded from these images.

5 Concluding remarks

We have formulated and numerically-implemented a coupled theory of electro-chemo-elasticity, and applied it to model the actuation response of ionic polymer-metal composites (IPMCs). We have estimated the material parameters appearing in our theory using experimental data for step-input voltages available in the literature, and shown that the predictions from our calibrated theory are in good agreement with other data obtained from experiments using sinusoidal voltage inputs. We have also demonstrated the utility of our simulation capability by conducting full three-dimensional simulations of:

- A bio-inspired "fin" which should be useful as a control surface for both underwater and aerial robotics applications.
- A gripper for use as an end-effector of a small low-mass robotic arm for pick-and-place operations.

While our study represents a reasonable advance in the modeling of IPMCs, it is far from complete. Predicting the deformation response or sensing signal of an IPMC is a difficult task, and at present there is no single all-encompassing predictive theory. In part this is due to the many possible different types of IPMCs — based on different compositions of the backbone ionomer, the nature of the counterions, and

the different solvents — and the variability in performance between samples of IPMC materials (cf., e.g., Nemat-Nasser, 2008; Jo et al., 2013; Minaian et al., 2021).

An important physical phenomenon that we have not considered in our work is the phenomenon of "back-relaxation" (cf., e.g., Asaka et al., 1995; Nemat-Nasser, 2008). As we noted in the Introduction section of this paper,[16] Nafion-based IPMCs with alkali metal cations invariably first bend towards the anode under a step voltage, and then relax back towards the cathode while the applied voltage is being maintained. In this paper we restricted our attention to the small time-scale response of IPMCs, and did not attempt to model this complex phenomenon of "back-relaxation" which occurs at long time scales. The generally accepted view for the physical mechanisms responsible for back-relaxation focus on the slow water flow within the ionomer (Shahinpoor and Kim, 2004). However, in our view, a clear explanation and a model for back-relaxation effects — that is widely agreed upon — is not yet available. Some physical mechanisms that need to be considered in modeling of back-relaxation and the long term response of IPMCs include:

- Diffusion of the solvent within the membrane, and across its boundaries because of dehydration effects.
- Viscoelasticity of the polymer membrane.
- Electro-chemical reactions at the interface of the membrane with the electrode.

We leave such a modeling effort to future work

Acknowledgements: A gift from Mercedes-Benz Research & Development North America, Inc. to carry out this research at MIT is gratefully acknowledged.

CRediT authorship contribution statement: Conceptualization: L.A. and S.N; Formal analysis: L.A. and S.N; Investigation: S.N., E.S. and LA; Methodology: S.N., E.S. and LA; Software: S.N. and E.S; Validation: S.N. and E.S; Visualization: S.N. and E.S; Writing-original draft: S.N. and E.S; Writing-review & editing: All co-authors.

Declaration of competing interest The authors declare that they have no known competing financial interests or personal relationships that could have appeared to influence the work reported in this paper.

A The numerical permittivity factor ε_{num}

In this Appendix we provide an additional discussion of the use of the numerical factor ε_{num} introduced in the Poisson equation (3.5). Specifically we study the effects of a variation in the value of ε_{num}.

We first solved a *purely electrochemical problem* using the setup described in Section 3.2 for the response of a cantilevered Nafion IPMC beam subjected to a step-voltage. That is, we suppressed the mechanics coupling in our model by setting $\Omega = 0$, while all other material parameters had the same values as that listed in Table 1. For this case, with $\varepsilon_{\text{num}} = 10^7$, Fig. 19 shows the variation of the normalized concentration of the cations $\bar{c}$ in the membrane at the instant when $\bar{c}$ just reaches 0 or 1 at the boundaries of the membrane. For this problem (with no mechanical coupling, $\Omega = 0$) we were able to obtain a converged solution, and resolve the boundary layers by using a highly refined mesh in the boundary regions; the data points at the nodes in our mesh are marked with x-symbols in Fig. 19. As is clear from this figure there exist two boundary layers — one close to the top surface of the membrane and one near the bottom surface. The thickness of these boundary layers is in the $\approx 5\mu$m range, which represents about $\sim 1.5\%$ of the total membrane thickness of 300μm.

[16] Cf. page 3.

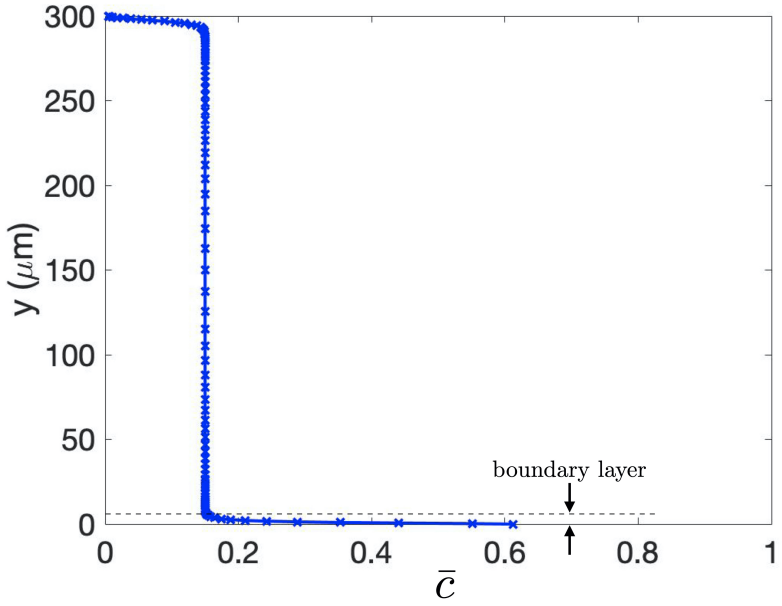

Figure 19: Variation of the normalized action concentration $\bar{c}$ across thickness of Nafion membrane for $\varepsilon_{\text{num}} = 10^7$ and $\Omega = 0$.

Next, we repeated the calculation but this time with $\varepsilon_{\text{num}} = 10^5$. In this case, the variation in cation concentration $\bar{c}$ in the membrane is shown in Fig. 20. The widths of layers are now considerably smaller, as compared to Fig. 19. The mesh for this simulation had to be refined so that the boundary layers was resolvable. As expected the boundary layer widths with $\varepsilon_{\text{num}} = 10^5$ are $\approx 0.5\mu$m — about an order of magnitude smaller than the widths when $\varepsilon_{\text{num}} = 10^7$. This change is in agreement with the numerical Debye length eq. (3.6).

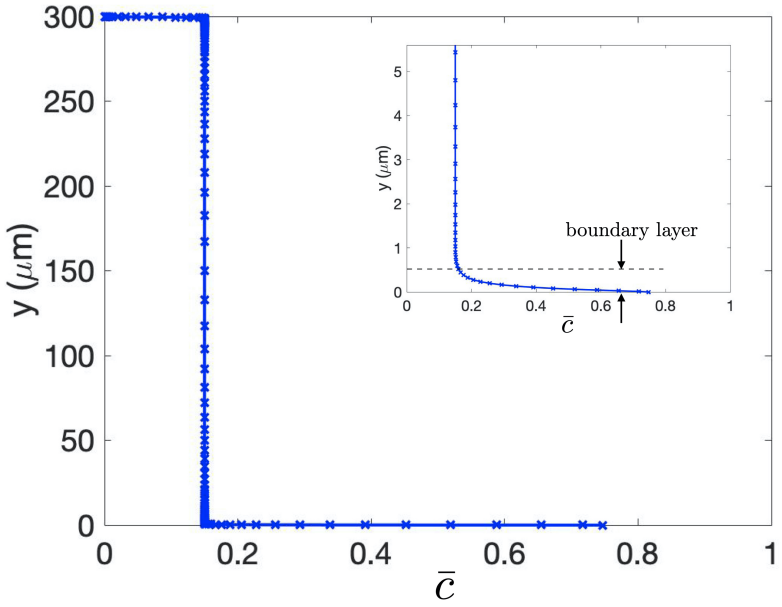

Figure 20: Normalized concentration variation across thickness of Nafion membrane for $\varepsilon_{\text{num}} = 10^5$. The inset shows a closer view of the boundary layer that forms at the bottom of the membrane.

Similarly, when the calculation is successively carried out with $\varepsilon_{\text{num}} = 10^3$ and $\varepsilon_{\text{num}} = 10$, the boundary layers shrink even further in size. The variation in the cation concentration for the case of $\varepsilon_{\text{num}} = 10^3$ and 10 are shown respectively in Fig. 21(a) and (b) respectively. The insets in the corresponding plots show the size of the boundary layers.

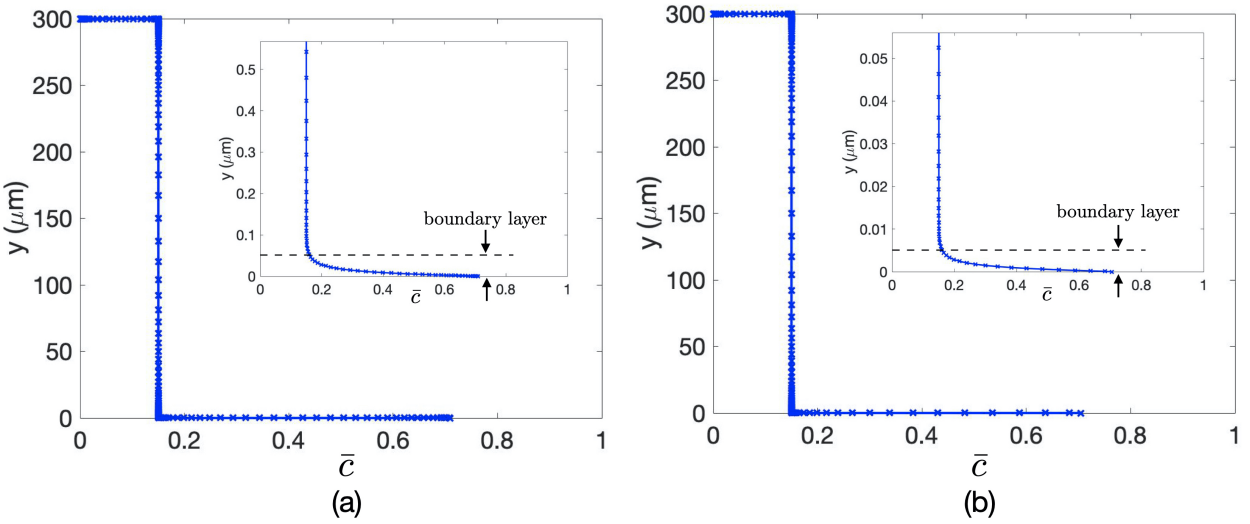

Figure 21: Normalized concentration variation across thickness of Nafion membrane for (a) $\varepsilon_{\text{num}} = 10^3$ and (b) $\varepsilon_{\text{num}} = 10^1$. The inset shows a closer view of the boundary layer that forms at the bottom of the membrane.

To summarize, the boundary layer widths from these calculations are:

$$\approx 5\,\text{nm for } \varepsilon_{\text{num}} = 10, \quad \approx 50\,\text{nm for } \varepsilon_{\text{num}} = 10^3, \quad \approx 500\,\text{nm for } \varepsilon_{\text{num}} = 10^5, \quad \text{and} \quad \approx 5\,\mu\text{m for } \varepsilon_{\text{num}} = 10^7.$$

In fact, with $\varepsilon_{\text{num}} = 1$ which corresponds to using the experimentally measured value of relative permittivity $\epsilon_r = 120$ of Nafion membranes in Gauss's law (Wallmersperger et al., 2008a), the boundary layer widths are only about 1.5 nm. Resolving boundary layers of widths 1.5 nm in a 300 micron thick membrane is computationally not tractable. Specifically, when the fully-coupled problem is solved with $\Omega \neq 0$, the small aspect ratio of quadrilateral elements significantly affects the solution to the fully-coupled problem — and it becomes computationally extremely expensive to resolve such thin boundary layers. Even a value of $\varepsilon_{\text{num}} = 10^5$ results in very sharp boundary layers ≈ 500 nm in thickness.

- It is for this reason that we have used a value of $\varepsilon_{\text{num}} = 10^7$ in our simulations. In this case the thickness of boundary layers is increased to the micron range, $\approx 5\,\mu$m, which represents $\sim 1.5\%$ of the total membrane thickness — and therefore resolvable with a computationally tractable number of finite elements.

Remarks:

1. Many researchers in their studies on Nafion-based IPMCs have used large numbers for the relative permittivity. Wallmersperger et al. (2008b), Nardinocchi et al. (2011), Galante et al. (2013), and Nardinocchi and Pezzulla (2013) have all used a value of $\varepsilon_r = 2 \times 10^9$, which is very different from the experimentally measured value $\varepsilon_r = 120$ reported by Wallmersperger et al. (2008a). Presumably, large values of ε_r have been used for aiding computational tractability, as discussed here. However, to the best of our knowledge, a justification for the use of ramped-up values of ε_r has not been previously given in the IPMC modeling literature.

2. More importantly, artificially increasing the value of ε_r for not only the Poisson equation but also for the Maxwell stress contribution to the Cauchy stress has an unintended consequence concerning the importance of the role of Maxwell stresses in the theory — possibly leading to unphysical conclusions. Indeed, Porfiri et al. (2017) in their study of back-relaxation in IPMCs used a large value of $\varepsilon_r = 5 \times 10^6$ and concluded that,

   > "Maxwell stress could be the critical explaining variable for back relaxation."

   But because of the large value of ε_r that they used in assessing the role of the Maxwell stress in their study, their conjecture is questionable.[17]

3. We reiterate that in our paper:

   - We have used the ε_{num} factor only in the Poisson equation (3.5).
   - We **do not** use this factor in equation (2.107) for the Cauchy stress, which would artificially enhance the effects of the Maxwell stress.

   Using a physically meaningful value of the electrical permittivity for calculating the Maxwell stresses is a key factor which enabled us to accurately model and predict the IPMC actuation experiments.

References

Abaqus. Abaqus standard, V 6.17. Simulia-Dassault Systèmes, 2017.

L. Anand. On H. Hencky's approximate strain-energy function for moderate deformations. *ASME Journal of Applied Mechanics*, 46:78–82, 1979.

K. Asaka, K. Oguro, Y. Nishimura, M. Mizuhata, and H. Takenaka. Bending of polyelectrolyte membrane–platinum composites by electric stimuli I. Response characteristics to various waveforms. *Polymer Journal*, 27(4):436–440, 1995.

Y. Cha and M. Porfiri. Mechanics and electrochemistry of ionic polymer metal composites. *Journal of the Mechanics and Physics of Solids*, 71:156 – 178, 2014.

S. A. Chester and L. Anand. A coupled theory of fluid permeation and large deformations for elastomeric materials. *Journal of the Mechanics and Physics of Solids*, 58(11):1879–1906, 2010.

S. A. Chester, C. V. Di Leo, and L. Anand. A finite element implementation of a coupled diffusion-deformation theory for elastomeric gels. *International Journal of Solids and Structures*, 52:1–18, 2015.

S. Galante, A. Lucantonio, and P. Nardinocchi. The multiplicative decomposition of the deformation gradient in the multiphysics modeling of ionic polymers. *International Journal of Non-Linear Mechanics*, 51:112–120, 2013.

M. E. Gurtin, E. Fried, and L. Anand. *The mechanics and thermodynamics of continua*. Cambridge University Press, 2010.

C. Jo, D. Pugal, I.-K. Oh, K. J. Kim, and K. Asaka. Recent advances in ionic polymer–metal composite actuators and their modeling and applications. *Progress in Polymer Science*, 38(7):1037 – 1066, 2013.

K. Kim and M. Shahinpoor. Ionic polymer-metal composites: II. Manufacturing techniques. *Smart Materials and Structures*, 12:65–79, 2003.

A. Kovetz. *Electromagnetic Theory*. Oxford University Press, 2000.

[17] Leronni and Bardella (2021) have recently emphasized the importance of the Maxwell stresses in their paper, but they too use large value of $\varepsilon_r = 1.12 \times 10^7$.

A. Leronni and L. Bardella. Modeling actuation and sensing in ionic polymer metal composites by electrochemo-poromechanics. *Journal of the Mechanics and Physics of Solids*, 148:104292, 2021.

N. Minaian, Z. J. Olsen, and K. J. Kim. Ionic polymer-metal composite (IPMC) artificial muscles in underwater environments: Review of actuation, sensing, controls, and applications to soft robotics. In D. A. Paly and N. M. Werely, editors, *Bioinspired Sensing, Actuation, and Control in Underwater Soft Robotic Systems*, pages 117–139. Springer, 2021.

P. Nardinocchi and M. Pezzulla. Curled actuated shapes of ionic polymer metal composites strips. *Journal of Applied Physics*, 113(22):224906, 2013.

P. Nardinocchi, M. Pezzulla, and L. Placidi. Thermodynamically based multiphysic modeling of ionic polymer metal composites. *Journal of Intelligent Material Systems and Structures*, 22(16):1887–1897, 2011.

P. Nardinocchi, M. Pezzulla, B. J. Akle, M. Guenther, and T. Wallmersperger. Actuation and buckling effects in IPMCs. In Y. Bar-Cohen, editor, *Electroactive Polymer Actuators and Devices (EAPAD) 2014*, volume 9056, pages 98 – 108. International Society for Optics and Photonics, SPIE, 2014.

S. Nemat-Nasser. Micromechanics of actuation of ionic polymer-metal composites. *Journal of Applied Physics*, 92(5):2899–2915, 2002.

S. Nemat-Nasser. Electrochemomechanics of ionic polymer-metal composites. In W. N. Sharpe, editor, *Springer Handbook of Experimental Solid Mechanics*, pages 187–201. Springer, 2008.

S. Nemat-Nasser and J. Y. Li. Electromechanical response of ionic polymer-metal composites. *Journal of Applied Physics*, 87(7):3321–3331, 2000.

S. Nemat-Nasser and C. W. Thomas. Ionomeric polymer-metal composites. In Y. Bar-Cohen, editor, *Electroactive Polymer (EAP) Actuators as Artificial Muscles: Reality, Potential, and Challenges*, volume PM 136, pages 171–230. SPIE Press, 2004.

V. K. Nguyen, J. W. Lee, and Y. Yoo. Characteristics and performance of ionic polymer–metal composite actuators based on Nafion/layered silicate and Nafion/silica nanocomposites. *Sensors and Actuators B: Chemical*, 120(2):529 – 537, 2007.

K. Oguro, Y. Kawami, and H. Takenaka. An actuator element of polyelectrolyte gel membrane-electrode composite. *Osaka Kogyo Gijutsu Shikensho Kiho*, 43(1):21–24, 1992.

V. Palmre, J. J. Hubbard, M. Fleming, D. Pugal, S. Kim, K. J. Kim, and K. K. Leang. An IPMC-enabled bio-inspired bending/twisting fin for underwater applications. *Smart Materials and Structures*, 22(1): 014003, 2013.

M. Porfiri, A. Leronni, and L. Bardella. An alternative explanation of back-relaxation in ionic polymer metal composites. *Extreme Mechanics Letters*, 13:78 – 83, 2017.

M. Rossi and T. Wallmersperger. Thermodynamically consistent three-dimensional electrochemical model for polymeric membranes. *Electrochimica Acta*, 283:1323 – 1338, 2018.

M. Rossi, T. Wallmersperger, J. A. Ramirez, and P. Nardinocchi. Thermodynamically consistent electro-chemo-mechanical model for polymer membranes. In Y. Bar-Cohen, editor, *Electroactive Polymer Actuators and Devices (EAPAD) XX*, volume 10594, pages 76 – 86. International Society for Optics and Photonics, SPIE, 2018.

A. Salvadori, D. Grazioli, M. Magri, M. Geers, D. Danilov, and P. Notten. On the role of saturation in modeling ionic transport in the electrolyte of (lithium ion) batteries. *Journal of Power Sources*, 294: 696–710, 2015.

M. B. Satterfield and J. B. Benziger. Viscoelastic properties of nafion at elevated temperature and humidity. *Journal of Polymer Science Part B: Polymer Physics*, 47(1):11–24, 2009.

M. Shahinpoor and K. J. Kim. Ionic polymer-metal composites: I. Fundamentals. *Smart Materials and Structures*, 10(4):819–833, 2001.

M. Shahinpoor and K. J. Kim. Ionic polymer–metal composites: III. Modeling and simulation as biomimetic sensors, actuators, transducers, and artificial muscles. *Smart Materials and Structures*, 13(6):1362–1388, 2004.

M. Shahinpoor, Y. Bar-Cohen, J. O. Simpson, and J. Smith. Ionic polymer-metal composites (IPMCs) as biomimetic sensors, actuators and artificial muscles - a review. *Smart Materials and Structures*, 7(6): R15–R30, 1998.

Z. Suo. Theory of dielectric elastomers. *Acta Mechanica Solida Sinica*, 23:449–578, 2010.

T. Wallmersperger, B. J. Akle, D. J. Leo, and B. Kröplin. Electrochemical response in ionic polymer transducers: An experimental and theoretical study. *Composites Science and Technology*, 68(5):1173 – 1180, 2008a.

T. Wallmersperger, A. Horstmann, B. Kroplin, and D. J. Leo. Thermodynamical modeling of the electromechanical behavior of ionic polymer metal composites. *Journal of Intelligent Material Systems and Structures*, 2008b.

L. A. Zook and J. Leddy. Density and solubility of nafion: Recast, annealed, and commercial films. *Analytical Chemistry*, 68(21):3793–3796, 1996.